Carbon Capture Science & Technology 13 (2024) 100252

Contents lists available at ScienceDirect

Carbon Capture Science & Technology

journal homepage: www.elsevier.com/locate/ccst

Full Length Article

# Boosting $CO_2$ separation in porphyrinic MOF-based mixed matrix membranes via central metal atom integration

Nicholaus Prasetya[a,*], Hasan Can Gülbalkan[b], Seda Keskin[b], Christof Wöll[a]

[a] Institute of Functional Interface (IFG), Karlsruhe Institute of Technology, Hermann-von-Helmholtz-Platz 1„ Eggenstein-Leopoldshafen 76344, Germany
[b] Department of Chemical and Biological Engineering, Koç University, Rumelifeneri Yolu, Sariyer, Istanbul 34450, Turkey

ARTICLE INFO

*Keywords:*
MOF-525
Post-Metalated MOF-525
Mixed matrix membranes
$CO_2$ separation

ABSTRACT

As atmospheric $CO_2$ levels continue to rise, contributing to the climate crisis, there is an increasing urgency to separate this gas from others and to expedite related research. Metal-Organic Frameworks (MOFs), known for their porosity and tunability, have already made significant impacts in this field, particularly to be used as part of a membrane material. This study introduces a novel method to enhance the $CO_2$ separation capabilities of MOFs-based mixed matrix membranes (MMMs). Instead of taking the traditional approach by functionalizing the MOF's ligands or varying the metal or metal-oxo MOF nodes, we harness the properties of metal atoms by integrating them as central elements within porphyrinic MOF linkers through a simple post-metalation method. As a result, by incorporating the post-metalated MOF-525 as fillers into the 6FDA-DAM (6FDA: 2,2-bis(3,4-dicarboxyphenyl)hexafluoropropane dianhydride; DAM: 2,4,6-trimethyl-1,3-diaminobenzene) polymer to fabricate MMMs, we effectively demonstrate improved $CO_2/N_2$ and $CO_2/CH_4$ gas separation capabilities of around 20 % without the necessity to use a very high MOF loading (only 2 wt%). Further analysis on the gas transport reveals that such a performance improvement mainly comes from the enhanced $CO_2$ solubility, which might be attributed to the presence of the metal atoms in the post-metalated MOF 525. Lastly, in order to get a more comprehensive understanding, we also carry out a computational study as a tool to validate and predict the experimental results of our MMMs. This study then opens up the possibility to further investigate the efficacy of introducing various metal atoms in other porphyrinic MOFs when they are used as fillers to significantly boost the $CO_2$ separation performance of MMMs.

## 1. Introduction

With the continuous rise of $CO_2$ concentration in the atmosphere that contributes to the climate crisis, the separation process of the $CO_2$ from other gases becomes crucial to effectively address the issue to avoid the release of this gas into the atmosphere. Compared to conventional technologies such as amine absorption, which is energy intensive, membrane technology could be a promising option in the future [Riboldi and Bolland, 2017, Anselmi et al., 2019, Fu et al., 2022].

Despite this huge promise, research and development in the field of advanced membrane materials is still required in order to improve the membrane separation performance [Fu et al., 2022]. Typically, economic factors and ease of processability make various polymeric materials the preferred choice for membrane construction. However, the performance of a polymeric membrane is usually limited by the permeability-selectivity inverse relationship [Robeson, 2008]. As a result, a membrane with high permeability usually exhibits low selectivity and vice versa. Consequently, the last few decades have seen the development of numerous new membrane materials, including polymers of intrinsic microporosity (PIM) [Wang et al., 2022], thermally-rearranged polymers [Bandehali et al., 2021] and metal organic frameworks (MOFs) [Qian et al., 2020]. Compared to polymeric materials, MOFs offer a number of advantages including high porosity, high surface area, tailorable architecture and also the possibility be used as a template for a new material [Qian et al., 2020, Petit, 2018, Pilz et al., 2023]. Therefore, during the last two decades, these crystalline coordination networks have been widely investigated to be used for various applications such as water purification and gas separation processes [Prasetya et al., 2023, Jia et al., 2022, Demir et al., 2022].

In the field of membrane-based gas separation processes, one of the most common strategies to harness the advantages offered by MOFs is to incorporate them as fillers in form of mixed matrix membranes (MMMs). In this case, MOFs act as the discrete phase that is uniformly dispersed within a polymer acting as the continuous matrix. By using this strategy, one can significantly improve the gas separation performance of a bare polymeric membrane because of the presence of the MOFs while also

* Corresponding author.
*E-mail address:* nicholaus.prasetya@partner.kit.edu (N. Prasetya).

https://doi.org/10.1016/j.ccst.2024.100252
Received 20 May 2024; Received in revised form 3 July 2024; Accepted 13 July 2024
2772-6568/© 2024 The Author(s). Published by Elsevier Ltd on behalf of Institution of Chemical Engineers (IChemE). This is an open access article under the CC BY-NC-ND license (http://creativecommons.org/licenses/by-nc-nd/4.0/)

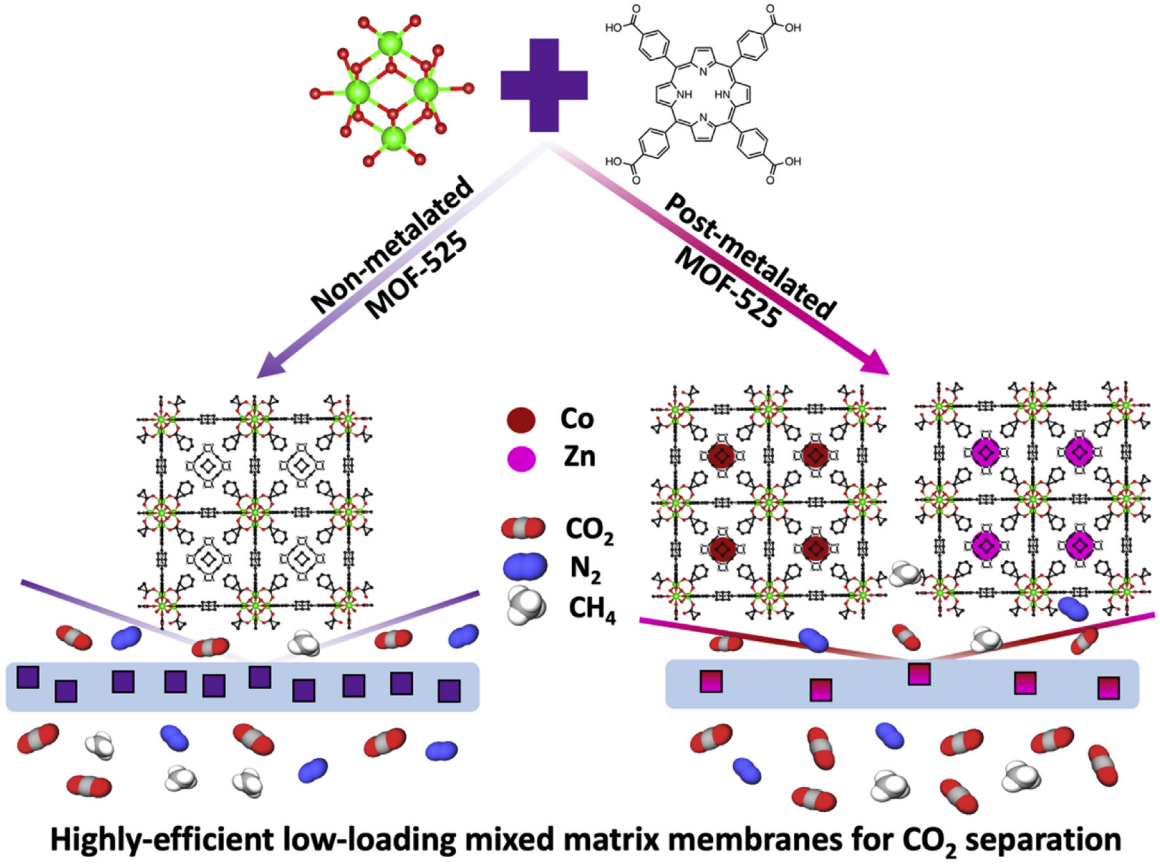



**Fig. 1.** An illustration of the post-metalation strategy of MOF-525 to improve the $CO_2$ separation performance in mixed matrix membranes.

keeping the advantages offered by a polymeric membrane, such as ease of processing and membrane handling [Prasetya et al., 2020, Zha et al., 2024]. However, judiciously choosing the MOFs as the filler is a crucial step in order to ensure the efficacy of the resulting MMMs.

In regard to the $CO_2$ separation, MOFs with polar functional groups [Xie et al., 2019, Babarao et al., 2011, Dasgupta et al., 2015, Li et al., 2020, Ge et al., 2024] or open metal sites [Li et al., 2020, Britt et al., 2009, Wongsakulphasatch et al., 2017, Kökçam-Demir et al., 2020] can be used as the common guideline to select the appropriate MOFs to be used as fillers in MMMs. This is because such MOFs can have better interaction with the $CO_2$ molecule and therefore, when incorporated inside a polymeric matrix, they could also contribute in enhancing the $CO_2$ affinity of resulting MMMs resulting in the gas separation performance improvement. Differing from these conventional approaches, this study aims to use a novel approach by employing porphyrinic MOFs and introducing transition metals in the porphyrinic MOFs through the post-metalation strategy. In fact, compared with the other approaches, this strategy could be more promising because, in addition to its simplicity and the possibility to maintain the properties of the parent MOF structure, one can also choose various possibilities of transition metals that will be introduced into the porphyrin ring to improve its $CO_2$ selectivity. There have then been a number of studies investigating the feasibility of this approach [Shang et al., 2022, Xu et al., 2015]. For example, this approach has been proven from a theoretical point of view employing density functional theory (DFT) and Grand Canonical Monte Carlo (GCMC) simulation showing that the metalated porphyrins can act as the selective binding sites for $CO_2$ by exerting a strong Coulomb interaction with $CO_2$ and thus resulting in the enhancement of the $CO_2$ adsorption capacity [Xu et al., 2015].

Therefore, in this work, we aim to further exploit this simple yet promising strategy using porphyrinic MOF-525, which are post-metalated with cobalt (Co) and zinc (Zn) and used as fillers to boost the performance of the MMMs formed by using 6FDA-DAM as the polymeric matrix. We hypothesize that the post-metalation process of MOF-525 could positively impact the $CO_2$ separation performance of the 6FDA-DAM by enhancing the interaction of the resulting MMMs with the $CO_2$ molecule. As illustrated in the Fig. 1, by significantly improving the interaction with the $CO_2$ molecule, one could also expect that the post-metalated MOF-525 could act as highly-efficient MMMs fillers where the $CO_2$ separation performance improvement of the resulting MMMs could be achieved even at relatively low particle loading.

## 2. Materials and methods

### 2.1. Materials

Benzoic acid, cobalt chloride ($CoCl_2$), sodium hydrochloride, zinc chloride ($ZnCl_2$) and zirconyl chloride octahydrate ($ZrOCl_2{\cdot}8H_2O$) were purchased from Merck. Meso-tetra(4-carboxyphenyl)porphyrin ($H_4TCPP$) was purchased from BLD Pharmatech GmbH, Germany. Acetone, dichloromethane, dimethylformamide (DMF), hydrochloric acid 37 % was purchased from VWR. 6FDA-DAM with molecular weight around 215,000 was purchased from Akron Polymer Systems, Inc.

### 2.2. MOF 525 synthesis and post-metalation of MOF-525

MOF-525 was synthesized according to the published procedure using benzoic acid as the modulator [Yu et al., 2020, Prasetya and Wöll, 2023]. In a typical synthesis condition, 750 mg of $ZrOCl_2{\cdot}8H_2O$ and 9 g of benzoic acid were firstly dissolved in a 50 mL DMF. Once a clear solution was obtained, 250 mg of $H_4TCPP$ was added to the

solution and the solution was sonicated for about 10 min to fully dissolve the ligand. The solvothermal process was then carried out by heating the solution in a convective oven at 100 ˚C for 24 h. Once the solvothermal process finished, the product was collected by centrifugation (7000 rpm) and washed thoroughly with DMF and acetone and dried at 80 ˚C overnight. The obtained particles (200 mg) were then immersed in a mixture of 20 mL DMF and 1 mL of 8 M HCl in an oven at 100 ˚C for 24 h to remove the ligated benzoates from the framework [Deria et al., 2016]. Afterwards, the MOF-525 was thoroughly washed with DMF and acetone and stored in acetone.

In order to post-metalate MOF-525, cobalt and zinc were used as the metal to be incorporated at the center of the porphyrin ring. Both metals were chosen because of the reproducibility for the post-metalation process. MOF-525 was then post-metalated according to the published procedure [Kung et al., 2015, Prasetya and Okur, 2023, Herrera-Herrera et al., 2021, Morris et al., 2012]. In a typical post-metalation process, a 20 mL DMF solution containing 1.24 mmol of the chloride salt of the metal ($CoCl_2$ and $ZnCl_2$) was firstly prepared. Afterwards, 100 mg of the MOF-525 was immersed in the solution followed by heating the suspension in a convective oven at 100 ˚C for 48 h. Once the post-metalation process was completed, the samples of the post-metalated MOF-525 was washed thoroughly with DMF and acetone. As in the case of MOF-525, the samples were always stored in acetone before being used as the fillers in the mixed matrix membranes.

### 2.3. Mixed matrix membrane (MMM) fabrication

Mixed matrix membranes containing free-base MOF-525, MOF-525(Co) and MOF-525(Zn) were fabricated by using 6FDA-DAM as the polymer matrix. To construct the mixed matrix membranes (MMMs), a suspension was initially prepared using dichloromethane as the solvent. This mixture contained a specific amount of the chosen MOF and about 50 % of the total polymer. This suspension was firstly sonicated and vigorously stirred overnight in order to homogeneously disperse the MOF in the suspension and thus avoiding severe particle agglomerations and also to prime the MOF particles to enhance the MOF-polymer interaction. Afterwards, the rest of the polymer was added to the suspension and the final suspension was continuously stirred overnight. In a typical MMM fabrication, the total mass of the MOF and the 6FDA-DAM inside this suspension was usually maintained around 0.25 g. Therefore, for example in the case of 2 wt% MMM, 5 mg of MOF-525 or post-metalated MOF-525 and 0.12 g of 6FDA-DAM were firstly suspended in the dichloromethane. After overnight priming, 0.125 g 6FDA-DAM was further added to the suspension followed by overnight stirring. To form a MMM, this suspension was then poured on a clean glass petri dish (diameter 60 mm) and was covered with perforated aluminum foil. The petri dish was kept in a fume hood to let the solvent evaporate. Once the solvent has completely evaporated, the MMM was peeled off from the petri dish and dried in a convective oven at 80 ˚C before the gas separation testing.

### 2.4. Gas separation performance testing

The gas separation performance of the membranes was evaluated by using the constant-volume variable-pressure method using $CO_2$, $N_2$ or $CH_4$ as the permeating gases. The membrane coupon was firstly mounted in a stainless-steel membrane test cell (Millipore, 47 mm). Afterwards, both the feed and permeate side of the membrane rig were vacuumed. The experiment was then conducted at 25 ˚C and by maintaining the feed pressure at 2 bar. The gas permeability is then calculated based on the gradient of the pressure change on the permeate side as read by the pressure transmitter (Wika S-20).

Since the gas transport through a polymeric membrane can be described by a solution-diffusion model, the diffusivity and solubility coefficient of the permeating gas can also be approximated based on the gas permeability using the Eq. (1).

$$P = D\ x\ S \tag{1}$$

where $P$, $D$ and $S$ is the gas permeability (in Barrer), gas diffusivity and gas solubility, respectively. The diffusion of the gas through the membrane is approximated by the time-lag method using the Eq. (2).

$$D = \frac{l^2}{6\theta} \tag{2}$$

where $l$ and $\theta$ is the membrane thickness and the time lag, respectively.

### 2.5. Characterizations

**UV–Vis spectroscopy**. The UV–Vis spectra of the digested samples were recorded by using Cary 5000 UV/Vis Spectrophotometer equipped with Cary Universal Measurement Accessory (UMA). For all cases, the digestion process of the MOF particles was carried out by immersing them in 1 M NaOH solution for 24 h.

**X-Ray Diffraction**. The powder X-ray diffraction (PXRD) pattern of the non-metalated and post-metalated MOF-525 were collected by using D8 A25 Da-Vinci Bruker XRD. The samples were measured between $2\theta$ 4–20˚. The same instrument was also used to record the XRD pattern of the MMMs. In this case, the MMMs were firstly immobilized on the sample holder by using a seal tape before the measurement took place.

**Fourier-transformed infrared spectroscopy**. The Fourier-transformed infrared (FTIR) spectra of both the MOFs and the MMMs were recorded by using Bruker Hyperion - Tensor in Attenuated Total Reflectance (ATR) mode. The measurement took place between the wavenumber 4000 - 400 $cm^{-1}$

### 2.6. Computational methodology

To deepen our understanding of the gas separation performance observed in the experiment, we conducted a computational simulation study as well. The aim of this investigation was to compare the experimental results with those derived computationally. To realize this objective, we initially calculated the gas permeability of the MOFs through molecular simulations, followed by combining the results with experimental polymer data, and finally using these values in the Maxwell model [Maxwell, 1873, Vinh-Thang and Kaliaguine, 2013].

The crystallographic information of MOF-525 structure was obtained from the literature [Gomez-Gualdron et al., 2014]. Using the "edit structure" tool provided in Mercury 2023.2.0 [Macrae et al., 2020], Co and Zn metals were placed in the center of the porphyrin ring of MOF-525. Subsequently, the Materials Studio Forcite module [Biovia, 2017] was utilized to optimize the geometry of the generated structures. The smart algorithm, which uses the steepest descent, adjusted basis set Newton-Raphson and quasi-Newton methods was used to find the lowest energy conformation, with a maximum iteration number of 10,000. The convergence tolerance was set to quality of ultra-fine (energy tolerance value of $2 \times 10^{-5}$ kcal/mol, displacement tolerance value of $10^{-5}$ Å, and force tolerance value of $10^{-3}$ kcal). The cell parameters were allowed to be optimized.

The gas uptakes and self-diffusivities were computed by performing Grand Canonical Monte Carlo (GCMC) and molecular dynamics (MD) simulations, respectively, in MOF-525, MOF-525(Co), and MOF-525(Zn) using the RASPA [Dubbeldam et al., 2016] simulation code version 2.0.37. Nonbonded interactions were defined using the Lennard-Jones (LJ) potential, with intermolecular interactions truncated at a distance of 13 Å. The potential parameters of the framework structures were obtained using the DREIDING [Mayo et al., 1990] force field. $CO_2$ was represented as a three-site rigid molecule with a Lennard-Jones 12–6 potential, with partial charges positioned at the center of each site [Potoff and Siepmann, 2001]. The TraPPE force field [Eggimann et al., 2014] was employed to derive the potential parameters for $CO_2$. $N_2$ was modeled as a three-site rigid molecule, where nitrogen atoms occupied two sites, and the third site was located at the center of mass

with partial charges [Murthy et al., 1980]. $CH_4$ was modeled as a single sphere [Martin and Siepmann, 1998]. Pair potentials between different atoms were calculated using the Lorentz-Berthelot mixing rules. The charge equilibration (Qeq) method [Rappe and Goddard, 1991] as implemented in RASPA was utilized to assign partial charges to MOF atoms and to calculate electrostatic interactions between gas molecules and MOF atoms, Long-range electrostatic interactions were accounted for using the Ewald summation method [Ewald, 1921].

MD simulations utilized the gas loadings acquired from the results of GCMC simulations conducted at 2 bar and 25 °C, which were used as inputs to compute the diffusion of $CO_2$, $N_2$, $CH_4$ gases in each MOF. In addition to 10,000 initialization and 10,000 equilibration cycles, a total of $4 \times 10^6$ production cycles were employed. The temperature was maintained constant using the NVT ensemble with the Nose-Hoover thermostat [Evans and Holian, 1985]. The mean square displacement of gas molecules was calculated, and the self-diffusion coefficients of $CO_2$, $CH_4$, and $N_2$ were determined by averaging the diffusivities computed in the x, y, and z directions, following Einstein's relation [Frenkel and Smit, 2023, Einstein, 1956]. $CO_2$, $CH_4$, and $N_2$ permeabilities were calculated at the feed condition of 2 bar, presuming the permeate side to be under vacuum [Erucar and Keskin, 2011], using the results of GCMC and MD simulations.

Previous research employing the Maxwell model [Maxwell, 1873], which depends on an ideal morphology approximation for gas permeation, has shown a good agreement between experimental and simulated gas permeabilities of several MOF-based MMMs [Erucar and Keskin, 2011, Budhathoki et al., 2019, Su et al., 2016]. Therefore, we predicted the gas permeabilities of MMMs using the Maxwell model as shown in the Eq. (3):

$$P_{mmm} = P_p \left[ \frac{n \times P_{MOF} + (1-n) \times P_p - (1-n) \times \Phi \times (P_p - P_{MOF})}{n \times P_{MOF} + (1-n) \times P_p + n \times \Phi \times (P_p - P_{MOF})} \right] \quad (3)$$

In the Maxwell model, $n$ is the geometry shape factor taken as 0.3, assuming sphere-like MOF particles and Φ is the volume fraction of the MOF particles in the polymer matrix. To calculate Φ in each wt% loading, densities of MOFs and polymer were used. $P_{MOF}$ is the gas permeability for the MOF computed by molecular simulations as explained above, $P_P$ is the gas permeability for the polymer and $P_{MMM}$ is the gas permeability for the MMM. The Maxwell model is applicable only to dispersions with low filler content (Φ <0.2), based on the assumption that the flux pattern around a particle remains unaffected by the presence of neighboring filler particles [Bouma et al., 1997]. Consequently, the distribution of fillers within the matrix does not influence the parameters of the Maxwell equation. The model relies on a two-phase morphology, thereby predicting permeabilities for an ideal MMM.

## 3. Results and discussions

### 3.1. Characterization of MOF and MMMs

The MOF-525 used in this study has been previously synthesized and fully characterized [Prasetya and Wöll, 2023]. The particle size of this

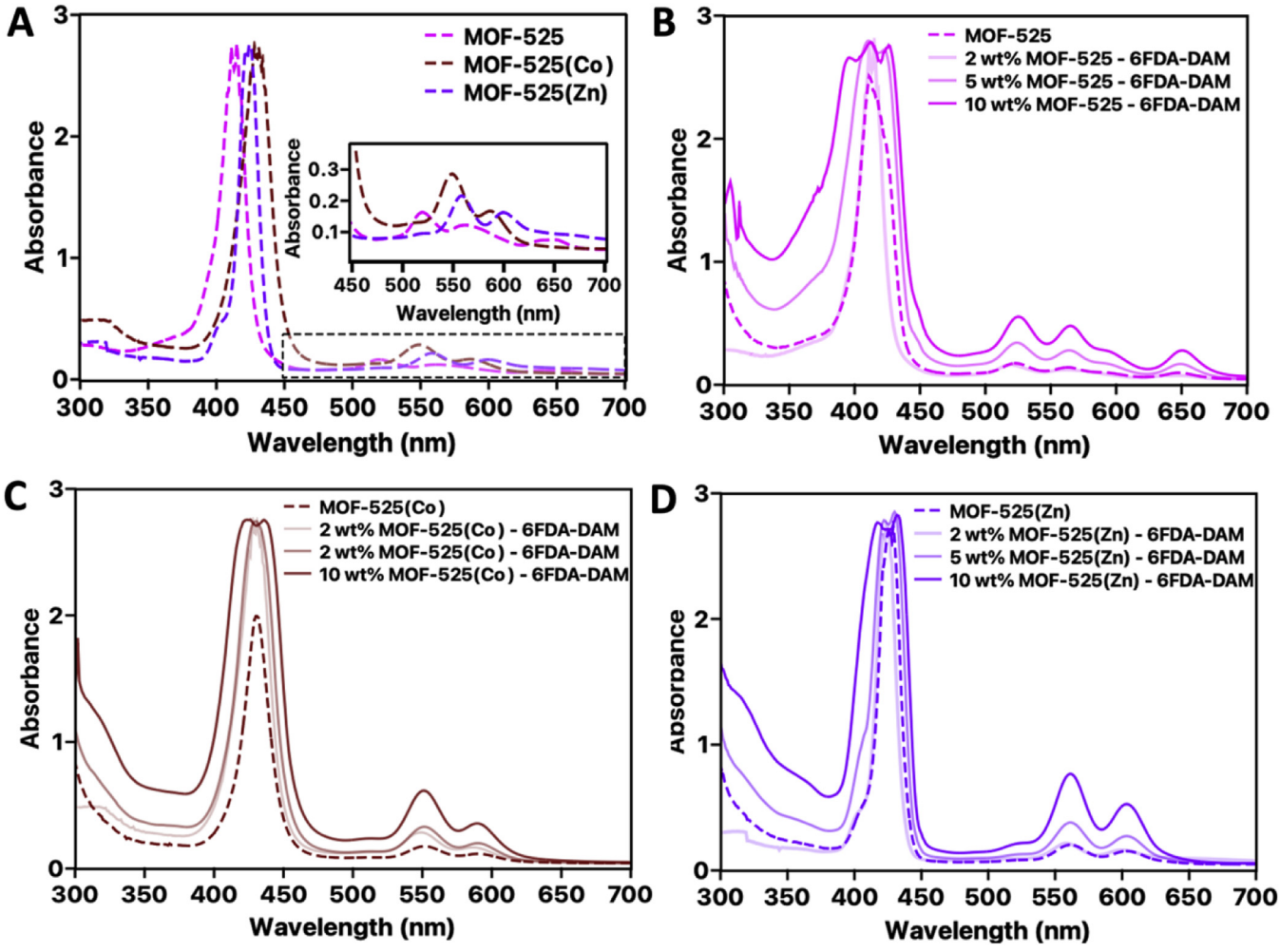



**Fig. 2.** The UV–Vis spectra of the digested MOF-525, MOF-525(Co) and MOF-525(Zn) (A), MOF-525 MMM (B), MOF-525(Co) MMM (C) and MOF-525(Zn) MMM (D).

MOF-525 is found to be around 200–300 nm (as also given in the Figure S1 in the Supporting Information) and its BET surface area is found to be around 1955 $m^2\ g^{-1}$ with the pore size distribution peaking at around 2 nm [Prasetya and Wöll, 2023]. The MOF-525 were then post-metalated with cobalt and zinc by immersing the MOF-525 particles in either a cobalt chloride or a zinc chloride DMF solution. This post-metalation process is neither expected to significantly alter the particle size (as can also be seen in the Figure S1 in the Supporting Information) nor significantly change the surface area and the pore size of the MOF-525, as has been previously studied [Morris et al., 2012]. However, such a post-metalation process could be expected to improve the interaction between the MOF-525 framework and the $CO_2$ molecules since the metal atoms in the porphyrin rings of the post-metalated MOF-525 could act as the selective binding sites for the $CO_2$ molecules [Xu et al., 2015]. Therefore, to firstly ensure the successfulness of the post-metalation process of the MOF-525, the UV–Vis spectrum of the digested MOF-525, MOF-525(Co) and MOF-525(Zn) was collected and the result is presented in Fig. 2(A). As can be seen from the result, the successfulness of the post-metalation process can be observed by the change of the UV–Vis spectrum of the MOF-525(Co) and MOF-525(Zn) from their non-metalated MOF-525, particularly in the wavelength around 400 nm, which corresponds to the Soret Band of the porphyrin ring and shifts to higher wavelength after the post-metalation. More prominently, in the region between 500 and 700 nm, which corresponds to the Q Band of the porphyrin ring, it can also be seen that there is a reduction from 3 bands found in the MOF-525 to 2 bands found both in MOF-525(Co) and MOF-525(Zn). Such a unique feature in a metalated porphyrin then proves the successfulness of the post-metalation process since the presence of a coordinated metal in a porphyrin brings a more symmetrical situation than in the case of free-base porphyrin and thus yielding in the simplification of the Q bands pattern [Giovannetti, 2012].

In addition, we also investigated the UV–Vis spectra of the digested MMMs to ensure that there is no alteration during the membrane fabrication process and the results are presented in the Fig. 2(B)-(D). As can be seen, the UV–Vis spectra of the MMMs are similar with the spectra of their corresponding MOF particles and thus indicating the absence of the alteration during the membrane fabrication process. Moreover, it can also be seen that the absorbance value of the MMMs corresponds to the loading of the particles and thus indicating the successfulness of the incorporation of the MOF particles inside the 6FDA-DAM matrix.

Having successfully proven the post-metalation process, the crystallinity of the MOF-525, MOF-525(Co) and MOF-525(Zn) was also inspected by collecting their PXRD pattern with the result is presented in the Fig. 3(A). As can be seen from the result, the PXRD peak of the non-metalated MOF-525 corresponds well with the simulated pattern. The same case can also be observed on the post-metalated MOF-525, namely MOF-525(Co) and MOF-525(Zn). This case is indeed expected since the post-metalation process is not expected to alter the crystal lattice of the MOF-525. However, it can also be seen that the peak relative intensity of MOF-525(Co) and MOF-525(Zn) is slightly different from MOF-525.

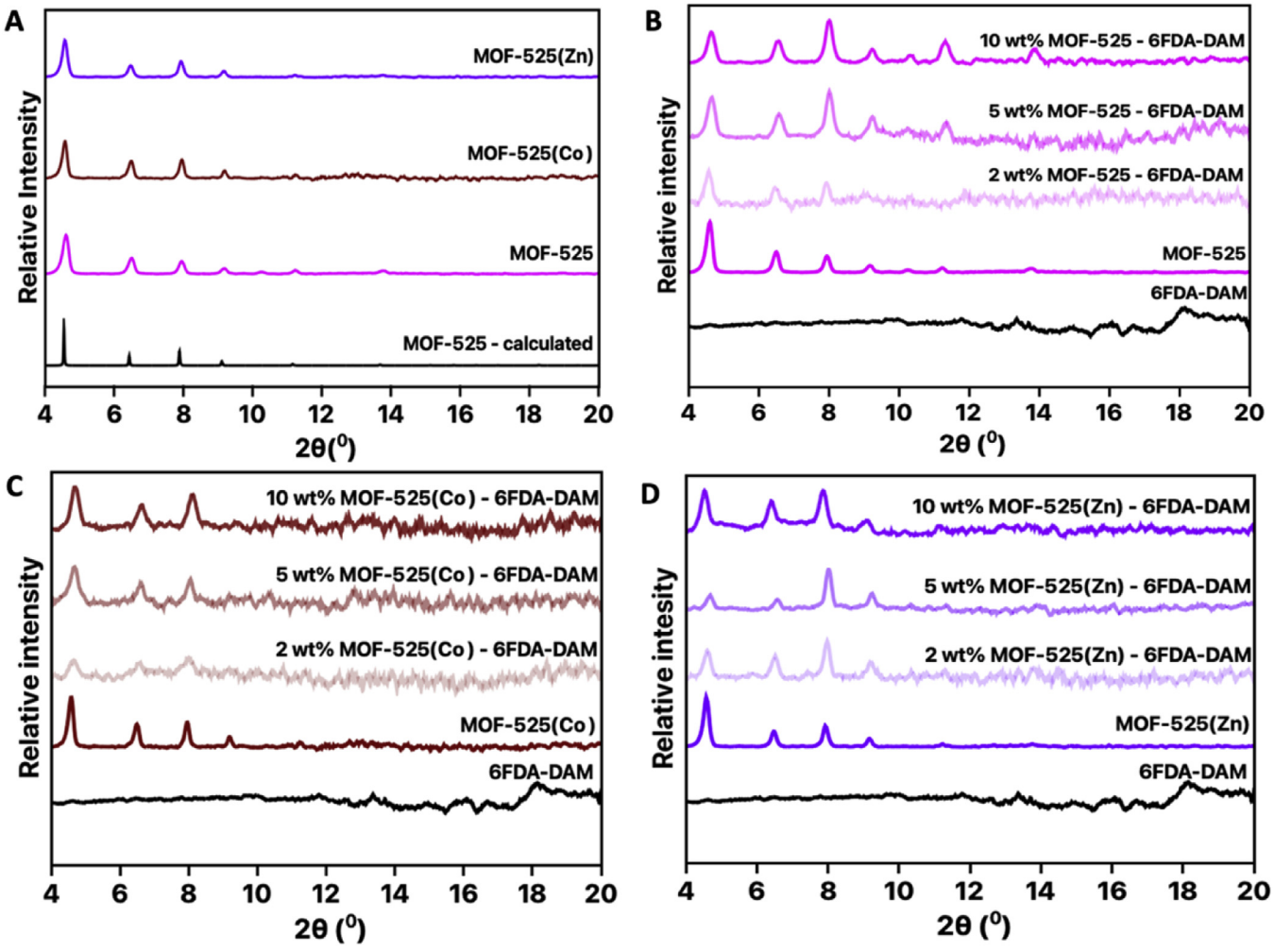



**Fig. 3.** The PXRD patterns of MOF-525, MOF-525(Co), and MOF-525(Zn) and the XRD patterns of the MOF-525 MMM (B), MOF-525(Co) MMM (C) and MOF-525(Zn) MMM (D).

This change of form factor after the post-metalation process is expected because of the change in electron density resulting from replacing the metals. [Prasetya and Wöll, 2023, Streit et al., 2012].

The XRD patterns of the MMMs were also collected in order to examine whether the MOF crystallinity can still be preserved during the MMM fabrication process since it involves impactful steps such as mechanical stirring. As can be seen in the results in the Fig. 3(B)-(D), for all cases, the peaks corresponding to the non-metalated and post-metalated MOF-525 start to appear at the lowest loading, namely 2 wt%, even though these peaks are relatively weak considering the relatively low particle loading in this case. However, as the particle loading inside the MMMs increases, the peak intensity also becomes higher and this becoming more prominent in the case of 10 wt% MMM. These results then successfully indicate that the crystallinity of all the MOFs can be well-preserved during the MMM fabrication process. This might then be attributed to the strong coordination bonding established between the Zr as a high-valence metal atom with the carboxylate ligand.

The FTIR spectra of the particles and the MMMs were also collected, and the results are presented in the Fig. 4(A)-(D). Firstly, from the Fig. 4(A), it can be seen that almost no difference can be observed between the non-metalated and post-metalated MOF-525. Meanwhile, for the case of the MMMs, it can be generally observed that the FTIR spectra of the MMMs consist of the FTIR spectra of both MOFs and the 6FDA-DAM. However, differing from the UV–Vis spectra and XRD patterns, almost no difference observed between the MMMs loaded with 2 wt%, 5 wt% or 10 wt% particles. This might be caused since some of the peaks from the MOFs and the 6FDA-DAM actually overlap.

Therefore, in order to have a better perspective for the characterization purpose, the FTIR difference spectra are also obtained at the wavenumber between 1600 $cm^{-1}$ and 400 $cm^{-1}$ by subtracting the FTIR spectra of the MMM with the FTIR spectra of the 6FDA-DAM. Fig. 5(A)–(C) then presents the results for this analysis. As can be seen, differing from the previous FTIR spectra, the fingerprint of the MOF-525 and post-metalated MOF-525 in the MMM can be more clearly seen. For all the cases, it can be observed that there is an increase in the peak intensity at the wavenumber around 1410 $cm^{-1}$, 650 $cm^{-1}$ and 480 $cm^{-1}$ as the particle loading inside the 6FDA-DAM gets higher. As previously observed in Zr-porphyrin MOFs, the peaks at wavenumber around 1410 $cm^{-1}$ and 650 $cm^{-1}$ could be attributed to the symmetric stretching of the carboxylate linkers and the stretching mode of the metal-ligand bonding, respectively [Prasetya and Wöll, 2023, Hadjiivanov et al., 2020].

Lastly, the micrographs of all MMMs were also captured to analyze the MOF particles distribution inside the 6FDA-DAM polymeric matrix and are shown in Fig. 6(A)-(I). From the micrographs, it can be seen that both the non-metalated and post-metalated MOF-525 can be quite homogeneously dispersed inside the polymeric matrix. However, this seems to only happen until the particle loading is 5 wt%. When the particle loading is further increased to 10 wt%, it can be observed that particle agglomeration becomes more prominent. In this case, they are clustered together and are not homogenously dispersed across the polymer matrix. Such conditions could then impart a negative impact to the

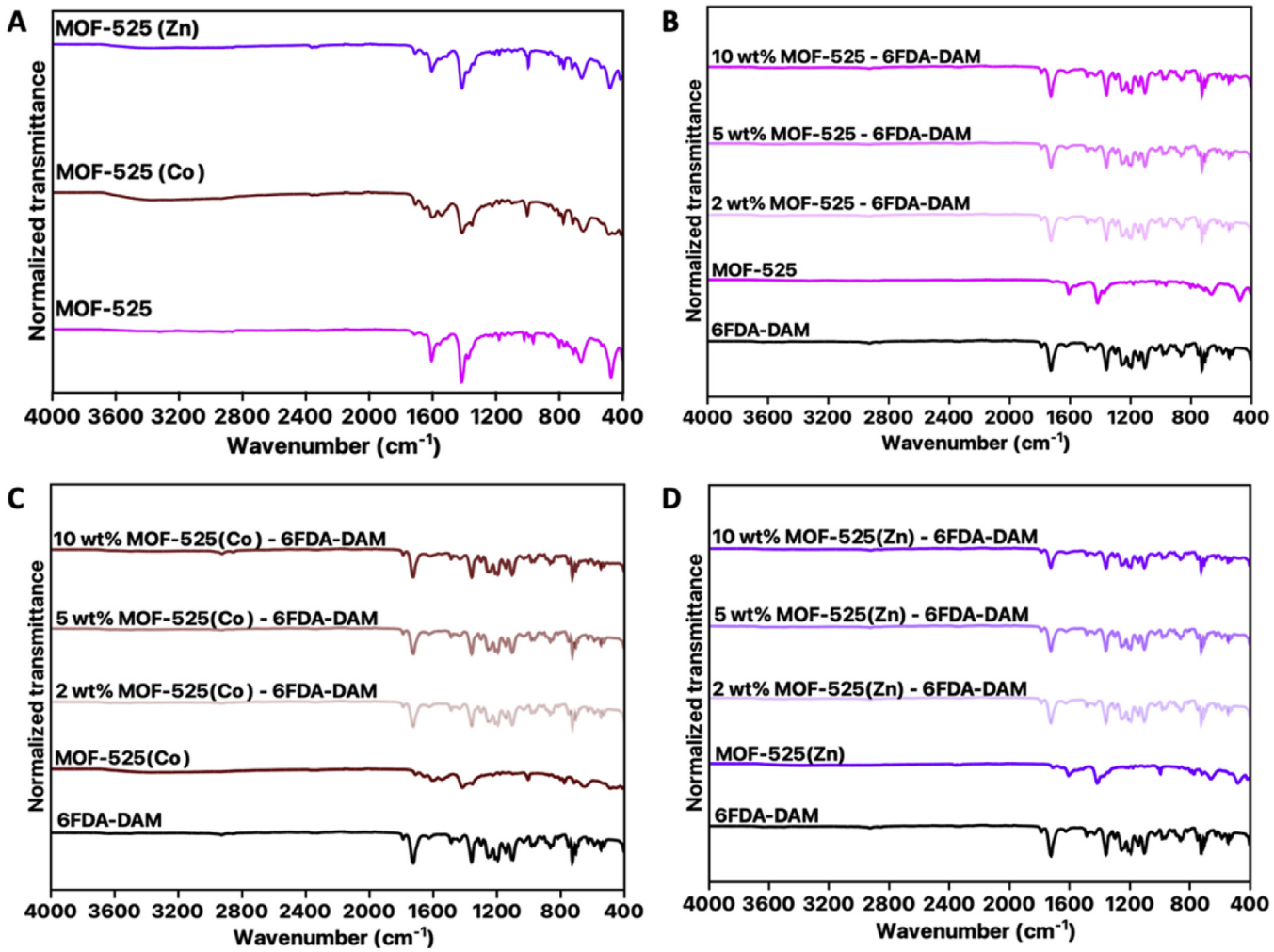



**Fig. 4.** The FTIR spectra of MOF-525, MOF-525(Co) and MOF-525(Zn) particles (A), MOF-525 MMM (B), MOF-525(Co) MMM (C) and MOF-525(Zn) MMM (D).

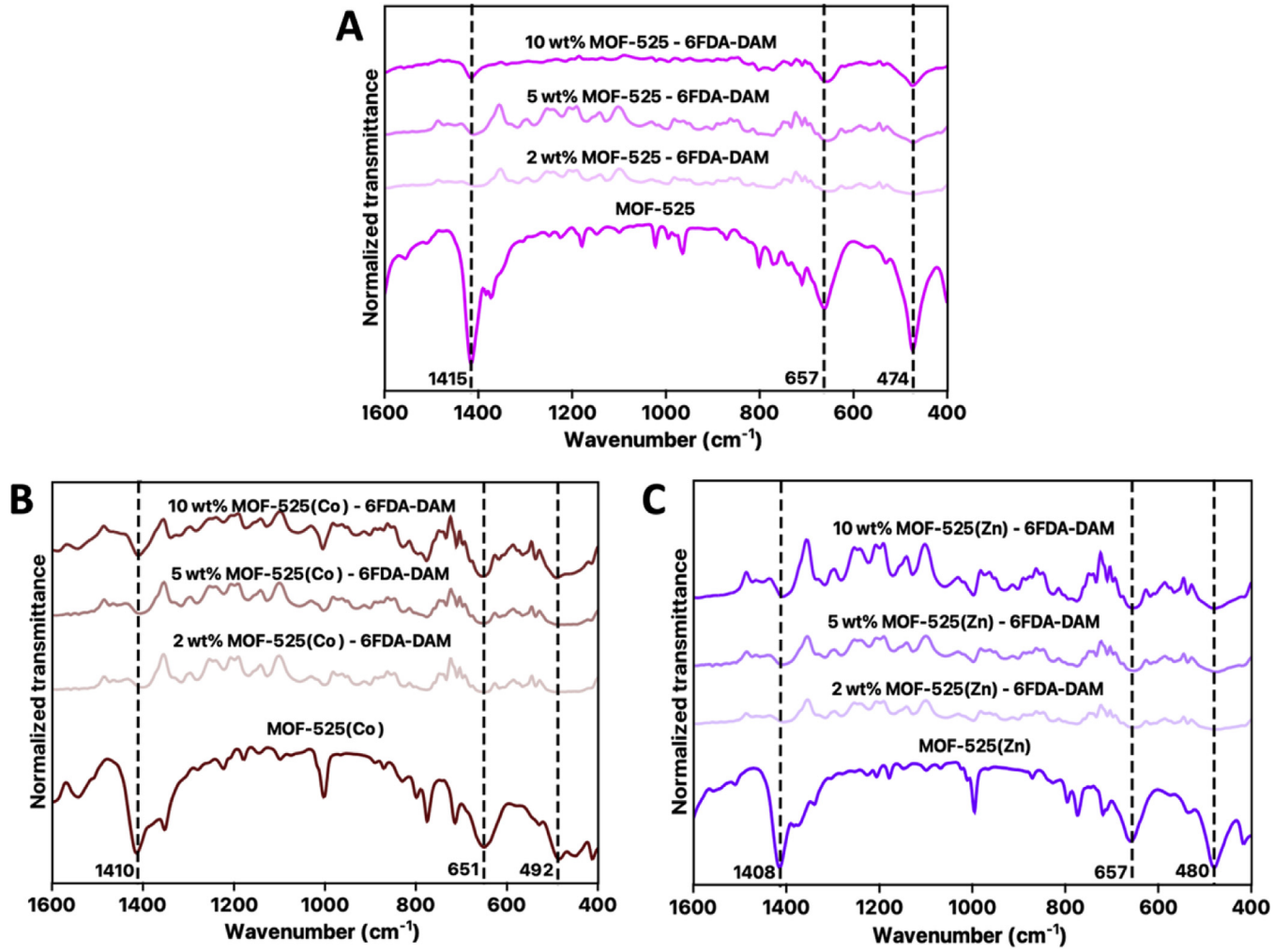



**Fig. 5.** The FTIR difference spectra of the MOF-525 MMM (A), MOF-525(Co) MMM (B) and MOF-525(Zn) (C).

separation performance of the MMMs, as will be further discussed in the next section.

### 3.2. $CO_2$ separation performance of MMMs

Having fully characterized the MOF particles and the MMMs, the $CO_2/N_2$ and $CO_2/CH_4$ separation performance of all MMMs were then evaluated and the results are given in the Fig. 7. Firstly, as can be seen from the Fig. 7(A) and (B), the $CO_2$, $N_2$ and $CH_4$ permeability of the bare polymeric membrane is found to be around 450, 27 and 25 Barrer, respectively. Therefore, the $CO_2/N_2$ and $CO_2/CH_4$ selectivity of the bare polymeric membrane is found to be around 17 and 18, respectively, which are also comparable with other reports [Chi et al., 2019, Altintas and Keskin, 2022, Maserati et al., 2017].

Once the polymer is loaded with 2 wt% of MOF particles, the increase of $CO_2$ permeability in all MMMs can be observed, which could be attributed to the additional gas pathway contributed by the MOF particles as they are embedded in the 6FDA-DAM. Therefore, such a trend becomes more prominent as more MOFs are added into the polymer matrix to reach 10 wt%. However, as can also be seen in the Fig. 7(A), differing from the trend of the $CO_2$ permeability, there is a tendency for the permeability of both gases to be stagnant when the MOF loading inside the MMMs is 5 wt% before a slight increase in their permeability occurs when the MOF loading is further increased to 10 wt%.

As a consequence of the differing trend of the gas permeabilities increase, a differing trend is also observed regarding the $CO_2/N_2$ and $CO_2/CH_4$ selectivity. As presented in the Fig. 7(B), higher MOF loading does not necessarily lead to improved $CO_2/N_2$ and $CO_2/CH_4$ selectivity. For all the cases, it can be seen that the $CO_2/N_2$ and $CO_2/CH_4$ selectivity for all MMMs reaches plateau at 5 wt% MMMs. Once the MOF particle loading inside both MMMs is further increased to 10 wt%, a decrease in gas selectivity can be observed and more prominent in the case of MOF-525(Co) and MOF-525(Zn) MMMs rather than MOF-525 MMM.

The diffusivity and solubility coefficient of the MMMs are then calculated to further analyze the gas transport and the results are depicted in Fig. 8(A) and (B), respectively. First, it can be seen that the $CO_2$ diffusivity of the bare 6FDA-DAM is found to be around $6.4 \times 10^{-7}$ cm$^2$ s$^{-1}$. Once loaded with the particles, a differing trend can be seen for each case of the MMM. For the MOF-525 MMM, an increasing trend of $CO_2$ diffusivity from the bare polymeric membrane can be observed from around $6.7 \times 10^{-7}$ cm$^2$ s$^{-1}$ for the 2 wt% MOF-525 MMM to be around $8.2 \times 10^{-7}$ cm$^2$ s$^{-1}$ for 10 wt% MOF-525 MMM. Meanwhile, in the case of MOF-525(Co) and MOF-525(Zn), such an increasing trend is not very prominent. In fact, for 2 wt% MOF-525(Co) and MOF-525(Zn) MMM, the $CO_2$ diffusivity slightly decreases from the bare polymeric membrane to be around $5.5 \times 10^{-7}$ cm$^2$ s$^{-1}$ and $5 \times 10^{-7}$ cm$^2$ s$^{-1}$, respectively. The $CO_2$ diffusivity of the 5 wt% MOF-525(Co) and MOF-525(Zn) MMM then increases to be around $5.8 \times 10^{-7}$ cm$^2$ s$^{-1}$ and $6.3 \times 10^{-7}$ cm$^2$ s$^{-1}$, respectively. A significant increase in the $CO_2$ diffusivity for the post-metalated MOF-525 MMM can be observed at the highest particle loading when it reaches $8.2 \times 10^{-7}$ cm$^2$ s$^{-1}$ and $1 \times 10^{-6}$ cm$^2$ s$^{-1}$ for MOF-525(Co) and MOF-525(Zn) MMM, respectively.

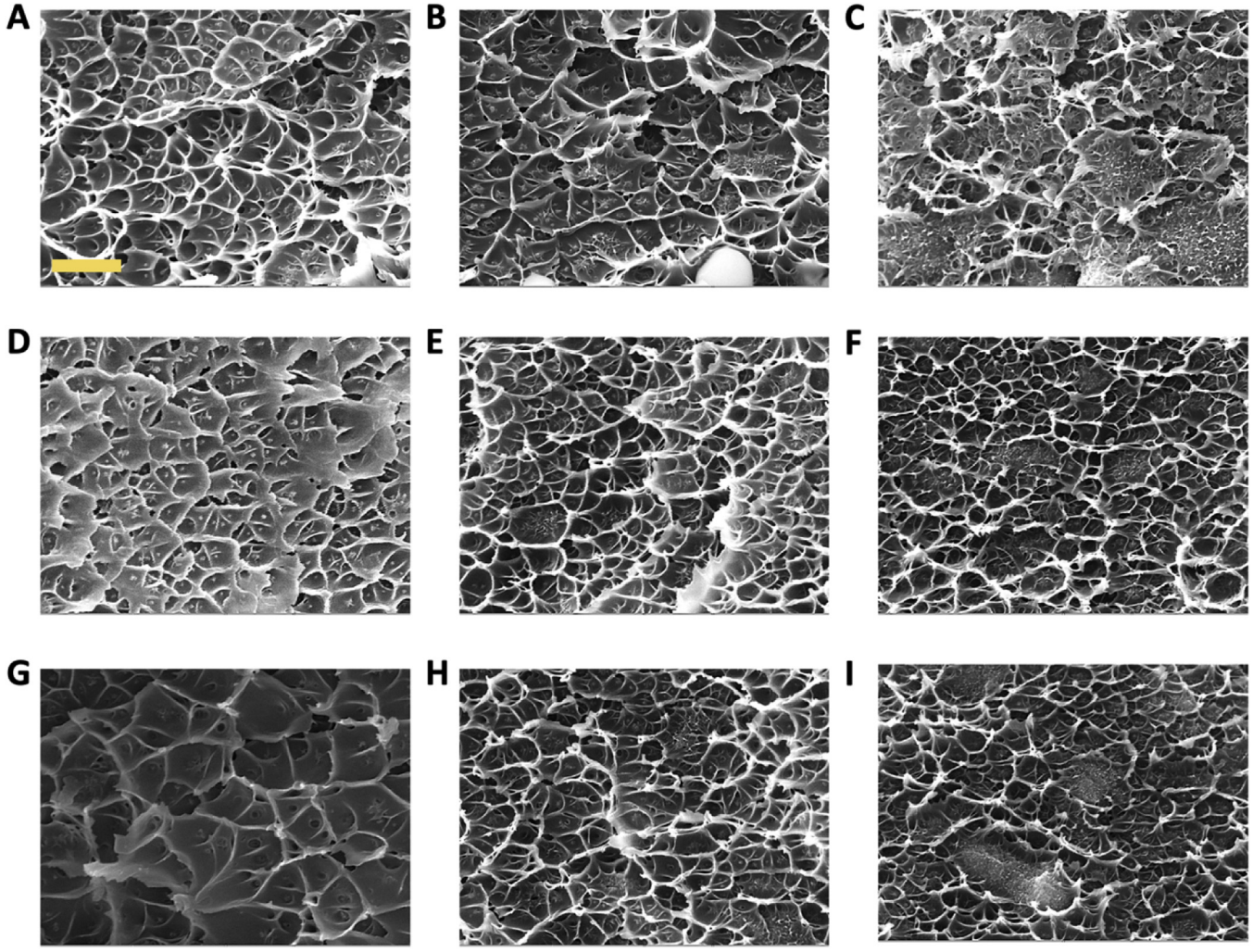



**Fig. 6.** SEM micrographs of 2 wt% (A), 5 wt% (B), 10 wt% (C) MOF-525 MMM, 2 wt% (D), 5 wt% (E) and 10 wt% (F)MOF-525(Co) MMM, 2 wt% (G), 5 wt% (H) and 10 wt% (I) MOF-525(Zn) MMM. The 5 $\mu$m scalebar for all the figures is given in (A).

As in the case with $CO_2$ diffusivity, there is also a differing trend regarding the $N_2$ and $CH_4$ diffusivity of the MMMs. For the 2 wt% MOF-525 MMM, the diffusion coefficient of both $N_2$ and $CH_4$ increases from $2.7 \times 10^{-7}$ $cm^2$ $s^{-1}$ and $1.2 \times 10^{-7}$ $cm^2$ $s^{-1}$ to be around $4 \times 10^{-7}$ $cm^2$ $s^{-1}$ and $1.5 \times 10^{-7}$ $cm^2$ $s^{-1}$, respectively. Differing from the MOF-525 MMM, there is no significant change observed regarding the $N_2$ and $CH_4$ diffusivity for both MOF-525(Co) and MOF-525(Zn) MMM. Upon further increase of the MOF loading to 5 wt%, the $N_2$ and $CH_4$ diffusivity for both MOF-525(Co) and MOF-525(Zn) MMM starts to increase to be around $4.3 \times 10^{-7}$ $cm^2$ $s^{-1}$ and $1.4 \times 10^{-7}$ $cm^2$ $s^{-1}$, respectively. At the highest particle loading, the $N_2$ and $CH_4$ diffusivity of all the MMMs show a significant increase from its bare polymeric membrane to be around $4.5 \times 10^{-7}$ $cm^2$ $s^{-1}$ and $2 \times 10^{-7}$ $cm^2$ $s^{-1}$, respectively.

Meanwhile, the $CO_2$ solubility of the 6FDA-DAM is found to be around $7 \times 10^{-2}$ $cm^3$STP $cm^{-3}$ $cmHg^{-1}$. Differing from the $CO_2$ diffusivity trend, an increase in the $CO_2$ solubility for all the cases of 2 wt% MMM can be observed. In this case, the $CO_2$ solubility of 2 wt% MOF-525, MOF-525(Co) and MOF-525(Zn) MMM is found to be around $7.8 \times 10^{-2}$ $cm^3$STP $cm^{-3}$ $cmHg^{-1}$, $9.1 \times 10^{-2}$ $cm^3$STP $cm^{-3}$ $cmHg^{-1}$ and $9.5 \times 10^{-2}$ $cm^3$STP $cm^{-3}$ $cmHg^{-1}$, respectively. However, such an increasing trend can no longer be observed at higher particle loading. At 5 wt% particles loading, the $CO_2$ solubility for MOF-525, MOF-525(Co) and MOF-525(Zn) MMM decreases to be around $7.1 \times 10^{-2}$ $cm^3$STP $cm^{-3}$ $cmHg^{-1}$, $8 \times 10^{-2}$ $cm^3$STP $cm^{-3}$ $cmHg^{-1}$ and $7.7 \times 10^{-2}$ $cm^3$STP $cm^{-3}$ $cmHg^{-1}$, respectively. A further decrease can then be seen for all the cases of 10 wt% MMM where the $CO_2$ solubility for MOF-525, MOF-525(Co) and MOF-525(Zn) MMM is found to be around $7 \times 10^{-2}$ $cm^3$STP $cm^{-3}$ $cmHg^{-1}$, $5.5 \times 10^{-2}$ $cm^3$STP $cm^{-3}$ $cmHg^{-1}$ and $5.4 \times 10^{-2}$ $cm^3$STP $cm^{-3}$ $cmHg^{-1}$, respectively.

In contrast to the $CO_2$ solubility trend, both $N_2$ and $CH_4$ solubility show a decreasing trend for all the case of the MMMs. The $N_2$ and $CH_4$ solubility of the bare 6FDA-DAM is found to be around $9.6 \times 10^{-3}$ $cm^3$STP $cm^{-3}$ $cmHg^{-1}$ and $2.1 \times 10^{-2}$ $cm^3$STP $cm^{-3}$ $cmHg^{-1}$, respectively. For the 2 wt% MMMs, the $N_2$ and $CH_4$ solubility decrease to be around $8.8 \times 10^{-3}$ $cm^3$STP $cm^{-3}$ $cmHg^{-1}$ and $2.2 \times 10^{-2}$ $cm^3$STP $cm^{-3}$ $cmHg^{-1}$, respectively. When the particle loading is increased to 5 wt%, the decrease in $N_2$ solubility is more pronounced in the case of MOF-525(Co) and MOF-525(Zn) MMM to be around $5.6 \times 10^{-3}$ $cm^3$STP $cm^{-3}$ $cmHg^{-1}$ in comparison to the MOF-525 MMM with $N_2$ solubility $7.4 \times 10^{-3}$ $cm^3$STP $cm^{-3}$ $cmHg^{-1}$. Meanwhile, the $CH_4$ solubility for all the 5 wt% MMMs is found to be around $1.5 \times 10^{-2}$ $cm^3$STP $cm^{-3}$ $cmHg^{-1}$. At the highest particle loading, the $N_2$ and $CH_4$ solubility of the MOF-525 MMM is found to be around $6.5 \times 10^{-3}$ $cm^3$STP $cm^{-3}$ $cmHg^{-1}$ and $1.6 \times 10^{-2}$ $cm^3$STP $cm^{-3}$ $cmHg^{-1}$, respectively. Meanwhile, the $N_2$ and $CH_4$ solubility values are found to be around $6 \times 10^{-3}$ $cm^3$STP $cm^{-3}$ $cmHg^{-1}$ and $1.2 \times 10^{-2}$ $cm^3$STP $cm^{-3}$ $cmHg^{-1}$, respectively, in the case of MOF-525(Co) and MOF-525(Zn) MMM.

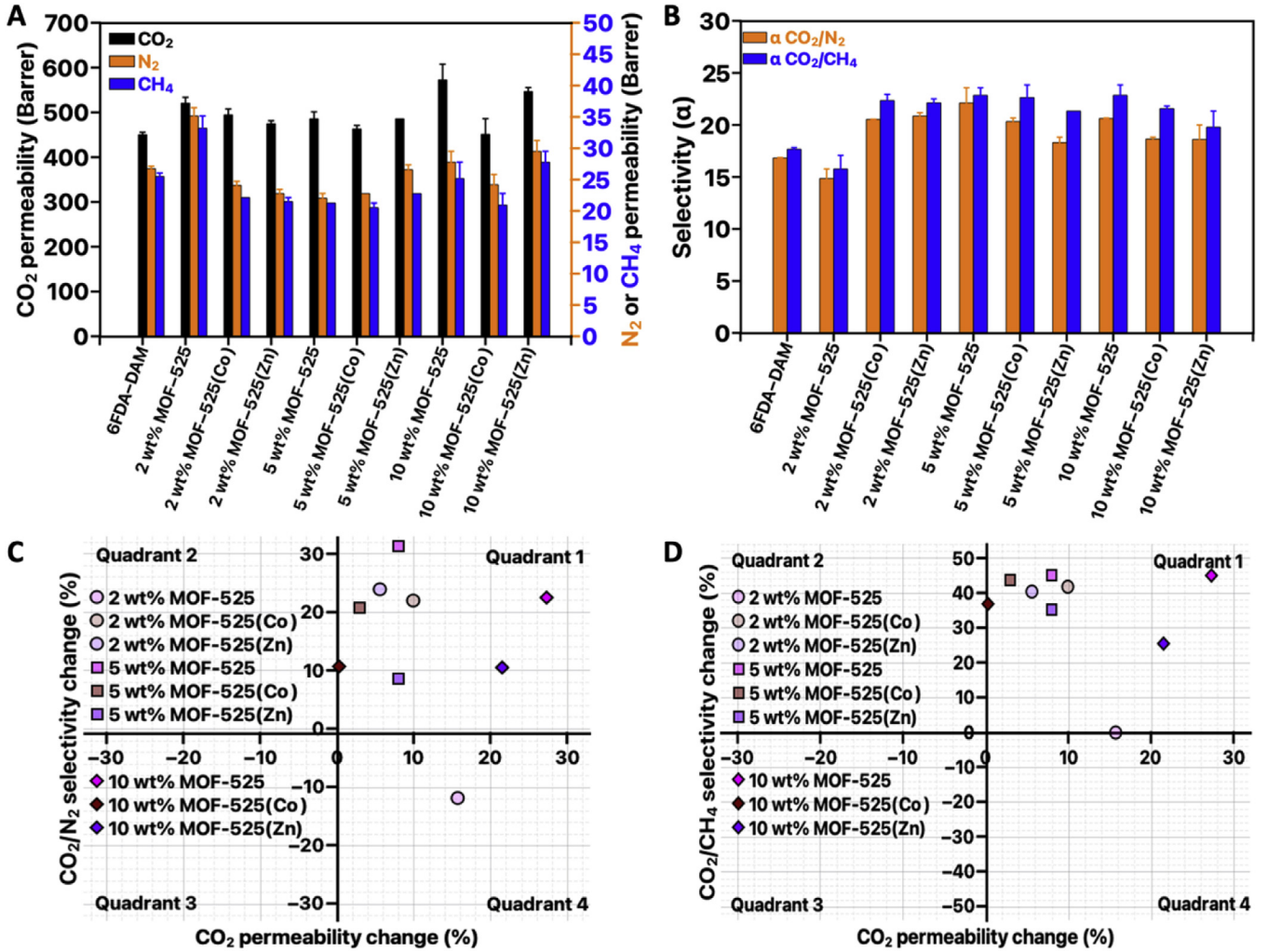



**Fig. 7.** The gas permeability (A) and $CO_2/N_2$ and $CO_2/CH_4$ selectivity (B) of the membranes. Figure (C) and (D) show the change of the $CO_2$ permeability and selectivity against $N_2$ and $CH_4$, respectively, of the MMMs against the 6FDA-DAM.

The differing trend of the diffusion and solubility coefficient exhibited by the MOF-525, MOF-525(Co) and MOF-525(Zn) MMMs then also result in the differing trend of their diffusivity and solubility selectivity, which is presented in the Fig. 8(C). The $CO_2/N_2$ and $CO_2/CH_4$ diffusivity selectivity of the bare 6FDA-DAM is found to be around 2.3 and 5.3, respectively. Meanwhile, the $CO_2/N_2$ and $CO_2/CH_4$ solubility selectivity of this membrane is found to be around 7.3 and 3.3, respectively. Once loaded with 2 wt% of the particles, there is barely any change observed regarding the diffusivity selectivity of all the MMMs. In contrast, a significant change can be observed in the solubility selectivity, more prominently in the post-metalated MOF-525 MMMs. In this case, the $CO_2/N_2$ and $CO_2/CH_4$ solubility selectivity of 2 wt% MOF-525(Co) can be significantly increased to be around 10 and 4.5, respectively. The same trend is also exhibited by the 2 wt% MOF-525(Zn) MMM where the values increase to be around 11.16 and 4.8, respectively.

When the particle loading is further increased to 5 wt%, it can be firstly seen that the diffusivity selectivity of the MOF-525 MMM changes slightly from the bare 6FDA-DAM. However, a significant improvement on the solubility selectivity can now be observed. In this case, the $CO_2/N_2$ and $CO_2/CH_4$ solubility selectivity of the 5 wt% MOF-525 MMM increases to be around 9.7 and 5.3, respectively. Meanwhile, in the case of 5 wt% MOF-525(Co) and MOF-525(Zn) MMM, the diffusivity selectivity is significantly lower than the bare 6FDA-DAM. The $CO_2/N_2$ and $CO_2/CH_4$ diffusivity selectivity for both MMMs are found to be around 1.4 and 4.3, respectively. In contrast, the solubility selectivity of both MMMs continues to increase in comparison to the 2 wt% MMM. The $CO_2/N_2$ and $CO_2/CH_4$ solubility selectivity are then found to be around 14 and 4.9, respectively.

Upon further increasing the particle loading to be 10 wt%, both the diffusivity and solubility selectivity of MOF-525 MMM show only a slight change in comparison to the 5 wt% MOF-525 MMM. A contrasting situation, on the other hand, can be seen in both 10 wt% MOF-525(Co) and MOF-525(Zn) MMM. In both cases, it can be seen that, although the diffusivity selectivity of both membranes barely changes, there is a significant decrease on the $CO_2/N_2$ and $CO_2/CH_4$ solubility selectivity for both membranes. For the 10 wt% MOF-525(Co) MMM, both values drop to be around 9.4 and 4.6, respectively. Meanwhile, the values for 10 wt% MOF are found to be around 8.6 and 4.5, respectively.

Analyzing from these results, it could then be firstly inferred that the improvement of $CO_2/N_2$ and $CO_2/CH_4$ selectivity for all the MMMs is likely caused by the improvement of the $CO_2$ solubility. This is firstly reflected in a slight decrease of the $CO_2$ diffusivity observed in the 2 wt% and 5 wt% MOF-525(Co) and MOF-525(Zn) MMMs which might be caused by the transient immobilization of the $CO_2$ during the permeation caused by the enhancement of the $CO_2$ sorption saturation, as previously observed in the case of CuTPA MMM [Adams et al., 2010]. This could occur since the interaction between the $CO_2$ molecule and both MOF-525(Co) and MOF-525(Zn) might be enhanced by the

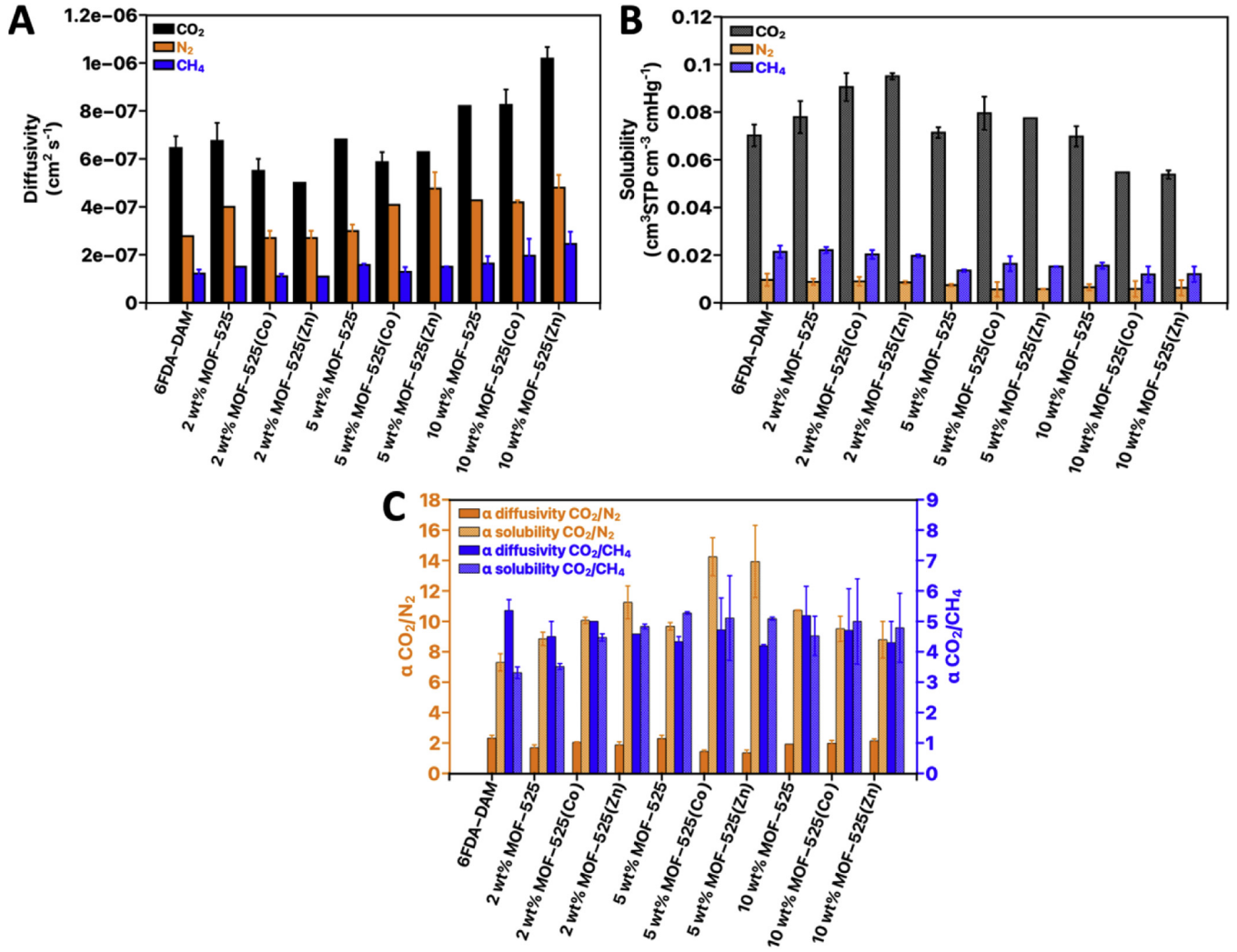



**Fig. 8.** The $CO_2$, $N_2$ and $CH_4$ diffusion (A) and solubility (B) coefficient and the $CO_2/N_2$ and $CO_2/CH_4$ diffusivity and solubility selectivity (C) of the membranes.

presence of the metal atoms in the porphyrin ring and thus contributing in hindering its diffusional process. In contrast, such a penetrant transient immobilization might only have limited impacts on both $N_2$ and $CH_4$ since their diffusivity in both 2 wt% and 5 wt% MOF-525(Co) and MOF-525(Zn) MMMs barely changes or slightly increases from the bare polymeric membrane. Such a phenomenon is then also clearly reflected by the prominent increase of the $CO_2$ solubility and $CO_2/N_2$ and $CO_2/CH_4$ solubility selectivity of the 2 wt% and 5 wt% MOF-525(Co) and MOF-525(Zn) MMMs while the value of the diffusivity selectivity barely changes or even decreases for some cases, such as in the case of 5 wt% MOF-525(Co) and MOF-525(Zn) MMM. This then highly indicates the beneficial aspect of employing post-metalated MOF as fillers in a MMM.

However, when the particle loading inside the polymeric matrix is increased to 10 wt%, the positive impact coming from the $CO_2$ solubility improvement is now impaired by the presence of non-selective defects in the MMM. Contrasting to the separation performance of both 2 wt% and 5 wt% MOF-525(Co) and MOF-525(Zn) MMMs, such a detrimental performance encountered in 10 wt% MOF-525(Co) and MOF-525(Zn) MMMs is very likely to be associated with the weakening interaction between the $CO_2$ molecule and the metal atoms in the porphyrin ring since the $CO_2$ molecule now preferentially permeates through the less-resistive and non-selective defective sites rather than the pores of the MOF-525(Co) and MOF-525(Zn), which is also clearly reflected by higher $CO_2$ diffusivity than the bare polymeric membrane and 2 wt% and 5 wt% MOF-525(Co) and MOF-525(Zn) MMMs. As a consequence, the penetrant transient immobilization, as observed in the case of 2 wt% and 5 wt% MOF-525(Co) and MOF-525(Zn) MMMs, does not occur and thus resulting in a decrease in both $CO_2$ solubility and solubility selectivity. This then results in the reduction of the $CO_2$ selectivity of the 10 wt% MOF-525(Co) and MOF-525(Zn) MMMs and thus causing them to have the lowest $CO_2$ selectivity when compared with the MMMs loaded with 2 wt% and 5 wt% MOF-525(Co) and MOF-525(Zn).

We also performed molecular simulations as a resource to offer valuable insights into gas permeation through MOF-based MMMs. Validating computational methodologies for predicting gas permeation through membranes necessitates comparing simulation results with experimental measurements for various separations. Molecular simulations of MOFs were conducted under identical pressure and temperature conditions as the experiments and then gas permeabilities were computed. The comparison of experimental $CO_2$, $CH_4$, and $N_2$ permeabilities of MMMs with the predictions of the Maxwell model are presented in the Fig. 9. From the results it can be seen that the Maxwell model overestimates the experimental gas permeabilities particularly at 5 wt% and 10 wt% loadings since particle agglomeration was observed in the experiments after 5 wt%. This is attributed to the assumptions that MOFs were modeled as defect-free crystals during molecular simulations and perfectly compatible within MMMs as considered in the Maxwell model [Vinh-Thang and Kaliaguine, 2013]. Recent studies have demonstrated that when the gas permeability of a polymer (approximately 450 Bar-

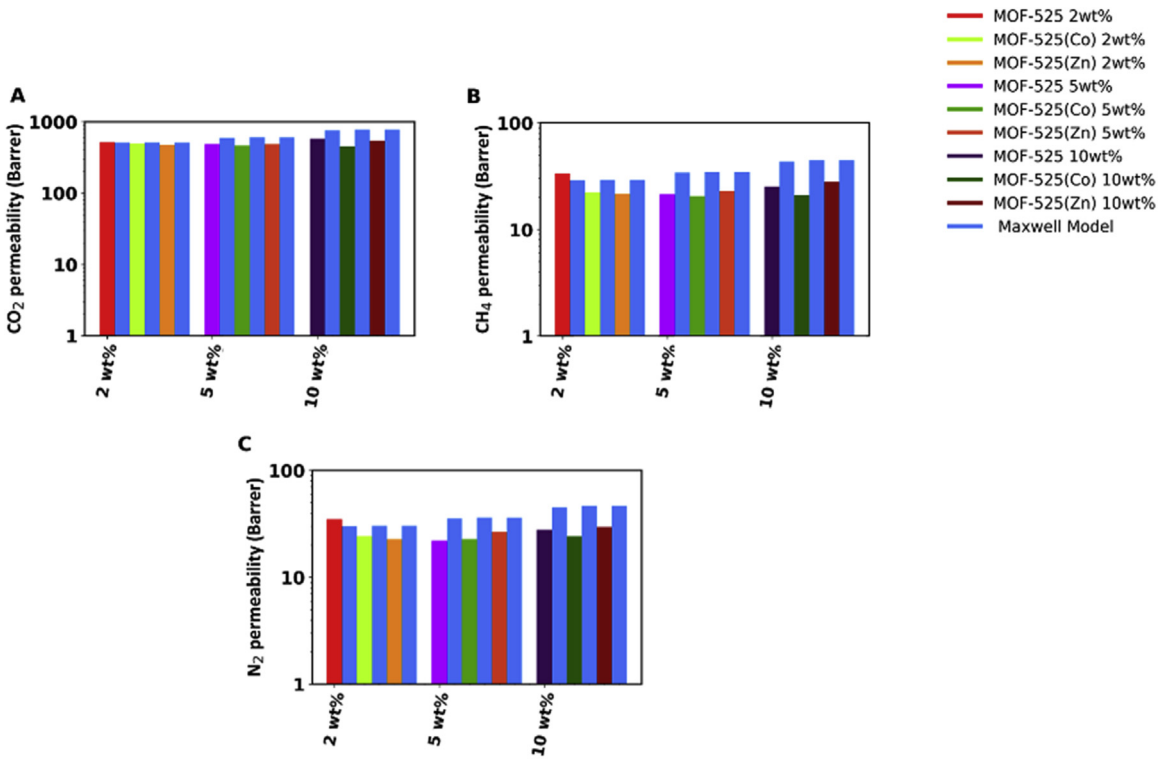



**Fig. 9.** Comparison of experimental pure gas permeabilities of $CO_2$ (A), $CH_4$ (B), and $N_2$ (C) in MOF-525, MOF-525(Co), and MOF-525(Zn)/6FDA-DAM MMMs with the predictions acquired from Maxwell model.

rer for $CO_2$) is significantly lower than that of pure MOF ($4.36 \times 10^4$ Barrer for MOF-525), the maximum gas permeability of the MMM calculated using the Maxwell model is up to two times higher than the permeability of the pure polymer [Budhathoki et al., 2019, Altintas and Keskin, 2018], which aligns with the results presented in the Fig. 9.

Lastly, to put the performance results of the MMMs used in this study into a perspective, their performance in relation to the upper bounds is also given in the Fig. 10 [Robeson, 2008, Comesaña-Gándara et al., 2019] and compared with other MOF MMMs used for $CO_2/N_2$ and $CO_2/CH_4$ separation [Chen et al., 2020, Deng et al., 2020, Gong et al., 2015, Prasetya and Ladewig, 2018, Mubashir et al., 2018, N. Prasetya et al., 2018, Benzaqui et al., 2017, Perez et al., 2009, Gao et al., 2020, Lai et al., 2019, Zornoza et al., 2011, Zhou et al., 2020, Rodrigues et al., 2018, Khdhayyer et al., 2017, H. Wang et al., 2021, Nik et al., 2012, Dorosti et al., 2014, Zhang et al., 2008, Y. Liu et al., 2018, Chen et al., 2012, Guo et al., 2015, Japip et al., 2014, Shahid and Nijmeijer, 2014, G. Liu et al., 2018, Guo et al., 2018, Z. Wang et al., 2021, Rodenas et al., 2014, Jiang et al., 2019, Qian et al., 2021, Castro-Muñoz et al., 2019, Jomekian et al., 2016, Bae and Long, 2013]. First, from the Fig. 10(A) and (C), it can be seen that the MMMs in this study is located at the lower right corner of the diagram and thus indicating a satisfactory $CO_2$ gas permeability, which is indeed an intrinsic feature of the 6FDA-DAM and thus can perform better than other MMMs fabricated with other glassy polymers such as Matrimid [Prasetya and Ladewig, 2018, Dorosti et al., 2014, Jiang et al., 2019, N. Prasetya et al., 2018] or polysulfone [Zornoza et al., 2011, Guo et al., 2015, Khan et al., 2022] that usually show a relatively low $CO_2$ permeability. Looking closely at the separation performance of the MMMs, it can be seen from the Fig. 10(B) and (D) that both the $CO_2/N_2$ and $CO_2/CH_4$ selectivity of the bare polymeric membrane can be enhanced so they are closer to the both 2008 and 2019 Upper Bound. However, the enhancement obtained by embedding the MOF-525 inside the matrix is not sufficient to surpass both upper bounds. This might then indicate that higher MOF loading might be necessary to simultaneously increase the gas permeability and selectivity. However, as has been previously discussed, there is a tendency for interfacial imperfections once the MOF loading reaches 10 wt% and thus a deterioration in membrane performance is very likely to be seen when the MOF loading is made higher. Despite this, it is worth to note that, in our case, only a relatively low loading of MOF particles in the range of 2–5 wt% is necessary to improve the performance of the bare polymeric membrane and thus resulting in the simultaneous improvement of gas permeability and selectivity. For example, as also illustrated in the Fig. 7(C) and (D), in the case of 2 wt% post-metalated MOF-525 MMM, the $CO_2$ permeability and selectivity against $N_2$ and $CH_4$ can be simultaneously improved up to 10 % and 25 %, respectively, to be around 494 Barrer and in the range of 20–22, respectively. Using the same polymer and ZIF-301, as an example, around 20 wt% of the particle loading is required to increase the $CO_2$ permeability and $CO_2/CH_4$ selectivity around 37.5 % and 31 %, respectively [Z. Wang et al., 2021]. In another investigation using polysulfone as a polymer, even though the $CO_2$ permeability of the membrane can be significantly increased up to more than 100 % using 16 wt% of ZIF-8 and HKUST-1, an improvement in $CO_2$ selectivity against $N_2$ and $CH_4$ can be barely observed [Zornoza et al., 2011]. This study has then clearly indicated the promising potential of employing porphyrinic MOFs particles to simultaneously improve the $CO_2$ permeability and selectivity of a polymeric membrane through the post-metalation strategy since the presence of the metal center in the porphyrin ring can increase the $CO_2$ solubility of the MMMs and thus improving their $CO_2$ solubility selectivity. This study has also highlighted the high-efficiency of this strategy since only a relatively low loading of particles is required to improve the membrane performance. Unfortunately, a non-ideal situation occurs at higher particle loading leading to interfacial defects and thus deteriorating the membrane performance. Therefore, if the interfacial defects issue can be solved, it could be expected that the performance of the resulting MMM could also be further enhanced by incorporating these particles. Moreover, another promising potential could also be expected if a porphyrinic MOFs with smaller pore aperture can be rationally

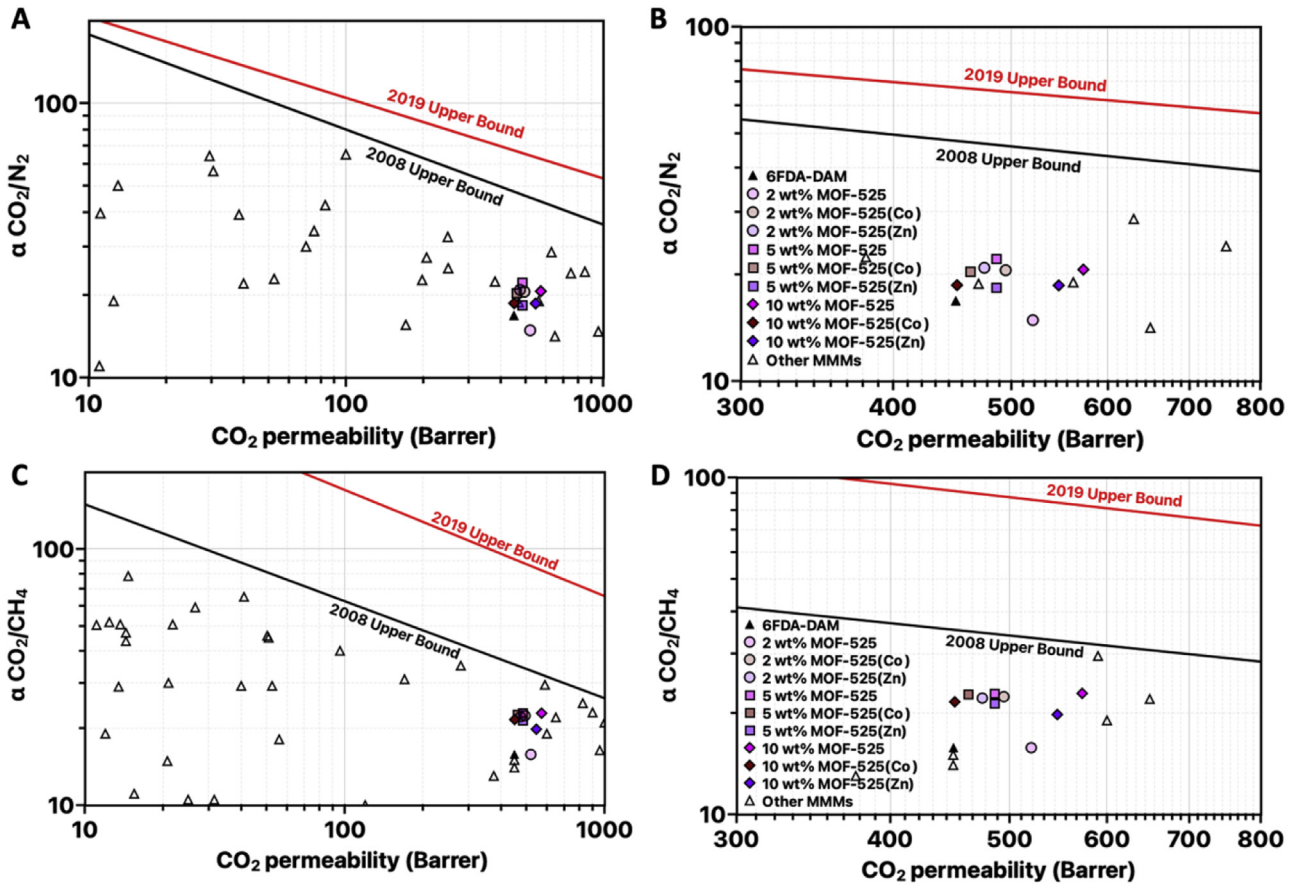



**Fig. 10.** The $CO_2/N_2$ (A and B) and $CO_2/CH_4$ (C and D) separation performance of the membranes used in this study evaluated against the 2008 and 2019 upper bound [Chen et al., 2020, Deng et al., 2020, Gong et al., 2015, Prasetya and Ladewig, 2018, Mubashir et al., 2018, N. Prasetya et al., 2018, Benzaqui et al., 2017, Perez et al., 2009, Gao et al., 2020, Lai et al., 2019, Zornoza et al., 2011, Zhou et al., 2020, Rodrigues et al., 2018, Khdhayyer et al., 2017, H. Wang et al., 2021, Nik et al., 2012, Dorosti et al., 2014, Zhang et al., 2008, Y. Liu et al., 2018, Chen et al., 2012, Guo et al., 2015, Japip et al., 2014, Shahid and Nijmeijer, 2014, G. Liu et al., 2018, Guo et al., 2018, Z. Wang et al., 2021, Rodenas et al., 2014, Jiang et al., 2019, Qian et al., 2021, Castro-Muñoz et al., 2019, Jomekian et al., 2016, Bae and Long, 2013]. The data for this graph can be seen in the Table S1 in the Supporting Information.

designed so the improvement does not only come from the improvement of $CO_2$ solubility but also diffusional selectivity.

## 4. Conclusions

In summary, our study has successfully demonstrated for the first time that introducing metal atoms in a porphyrinic MOF-525 through a simple post-metalation strategy can effectively turn the post-metalated MOF-525 into highly-efficient fillers to improve the $CO_2$ separation performance of MMMs. This has been clearly indicated by around 20 % improvement in both $CO_2/N_2$ and $CO_2/CH_4$ gas separation performance from the bare polymeric membrane observed in both MOF-525(Co)- and MOF-525(Zn)-MMMs, which can be achieved by loading the 6FDA-DAM only with 2 wt% fillers. However, the positive trend of the gas separation performance does not continuously increase with increasing particle loading. For the highest particle loading of 10 wt%, a slight decrease in the gas separation performance from the 5 wt% MMMs can be observed, indicating the presence of non-selective voids in the MMMs. Using molecular simulations and the Maxwell permeation model, gas permeabilities of the MMMs have been theoretically predicted and shown to overestimate the experiments, particularly at high particle loading. We speculate that the discrepancies between the experimental results and those predicted by the Maxwell model at high particle loading result from non-ideal conditions within the MOF MMM at the maximum loading used in this study. This observation underscores the importance of keeping the particle loading under 5 wt% for these specific MMMs, where conditions remain near-ideal, thereby allowing the Maxwell model to more accurately predict their gas separation performance. Therefore, if the issue of interfacial defects at high filler loading can be effectively addressed, the $CO_2$ separation performance of the MMMs using these post-metalated MOF-525 could then be further enhanced. More importantly, our study has also opened up the possibilities to further unleash the potential of other porphyrinic MOFs as fillers to boost the $CO_2$ separation performance of MMMs by introducing various metal atoms within their structure.

## Declaration of competing interests

The authors declare that they have no known competing financial interests or personal relationships that could have appeared to influence the work reported in this paper.

## CRediT authorship contribution statement

**Nicholaus Prasetya:** Writing – review & editing, Writing – original draft, Visualization, Validation, Supervision, Software, Resources, Project administration, Methodology, Investigation, Funding acquisition, Formal analysis, Data curation, Conceptualization. **Hasan Can Gülbalkan:** Writing – review & editing, Writing – original draft, Visualization, Validation, Software, Methodology, Investigation, Formal analysis, Data curation, Conceptualization. **Seda Keskin:** Writing – review & editing, Validation, Supervision, Software, Resources, Methodology,

Conceptualization. **Christof Wöll:** Writing – review & editing, Supervision, Resources, Project administration, Conceptualization.

## Acknowledgements

N. P acknowledges the funding from the Alexander von Humboldt Postdoctoral Fellowship (Ref 3.3 - GBR - 1219268 - HFST-P).

## Supplementary materials

Supplementary material associated with this article can be found, in the online version, at doi:10.1016/j.ccst.2024.100252.

## References


Riboldi, L., Bolland, O., 2017. Overview on pressure swing adsorption (PSA) as CO2 capture technology: state-of-the-art, limits and potentials. Energy Procedia 114, 2390–2400.

Anselmi, H., Mirgaux, O., Bounaceur, R., Patisson, F., 2019. Simulation of post-combustion CO2 capture, a comparison among absorption, adsorption and membranes. Chem. Eng. Technol. 42, 797–804.

Fu, L., Ren, Z., Si, W., Ma, Q., Huang, W., Liao, K., Huang, Z., Wang, Y., Li, J., Xu, P., 2022. Research progress on CO2 capture and utilization technology. Journal of CO2 Utilization 66, 102260.

Robeson, L.M., 2008. The upper bound revisited. J. Memb. Sci. 320, 390–400.

Wang, Y., Ghanem, B.S., Han, Y., Pinnau, I., 2022. State-of-the-art polymers of intrinsic microporosity for high-performance gas separation membranes. Curr. Opin. Chem. Eng. 35, 100755.

Bandehali, S., Amooghin, A.E., Sanaeepur, H., Ahmadi, R., Fuoco, A., Jansen, J.C., Shirazian, S., 2021. Polymers of intrinsic microporosity and thermally rearranged polymer membranes for highly efficient gas separation. Sep. Purif. Technol. 278, 119513.

Qian, Q., Asinger, P.A., Lee, M.J., Han, G., Mizrahi Rodriguez, K., Lin, S., Benedetti, F.M., Wu, A.X., Chi, W.S., Smith, Z.P., 2020. MOF-based membranes for gas separations. Chem. Rev. 120, 8161–8266.

Petit, C., 2018. Present and future of MOF research in the field of adsorption and molecular separation. Curr. Opin. Chem. Eng. 20, 132–142.

Pilz, L., Natzeck, C., Wohlgemuth, J., Scheuermann, N., Spiegel, S., Oßwald, S., Knebel, A., Braese, S., Wöll, C., Tsotsalas, M., 2023. Utilizing machine learning to optimize metal-organic framework-derived polymer membranes for gas separation. J. Mater. Chem. A.

Prasetya, N., Wenten, I.G., Franzreb, M., Wöll, C., 2023. Metal-organic frameworks for the adsorptive removal of pharmaceutically active compounds (PhACs): comparison to activated carbon. Coord. Chem. Rev. 475, 214877.

Jia, T., Gu, Y., Li, F., 2022. Progress and potential of metal-organic frameworks (MOFs) for gas storage and separation: a review. J. Environ. Chem. Eng., 108300.

Demir, H., Aksu, G.O., Gulbalkan, H.C., Keskin, S., 2022. MOF membranes for CO2 capture: past, present and future. Carbon Capture Sci. Technol. 2, 100026. doi:10.1016/j.ccst.2021.100026.

Prasetya, N., Himma, N.F., Sutrisna, P.D., Wenten, I.G., Ladewig, B.P., 2020. A review on emerging organic-containing microporous material membranes for carbon capture and separation. Chem. Eng. J. 391, 123575.

Zha, Z., Wang, J., Wang, Z., Zhao, S., 2024. Mixed-matrix membranes comprising porous organic molecular cage for efficient CO2 capture. Carbon Capture Sci. Technol. 10, 100152. doi:10.1016/j.ccst.2023.100152.

Xie, M., Prasetya, N., Ladewig, B.P., 2019. Systematic screening of DMOF-1 with NH2, NO2, Br and azobenzene functionalities for elucidation of carbon dioxide and nitrogen separation properties. Inorg. Chem. Commun. 108, 107512.

Babarao, R., Dai, S., Jiang, D., 2011. Functionalizing porous aromatic frameworks with polar organic groups for high-capacity and selective CO2 separation: a molecular simulation study. Langmuir 27, 3451–3460.

Dasgupta, T., Punnathanam, S.N., Ayappa, K., 2015. Effect of functional groups on separating carbon dioxide from CO2/N2 gas mixtures using edge functionalized graphene nanoribbons. Chem. Eng. Sci. 121, 279–291.

Li, Z., Liu, P., Ou, C., Dong, X., 2020. Porous metal–organic frameworks for carbon dioxide adsorption and separation at low pressure. ACS Sustain. Chem. Eng. 8, 15378–15404.

Ge, C., Sheng, M., Yuan, Y., Shi, F., Yang, Y., Zhao, S., Wang, J., Wang, Z., 2024. Pore-optimized MOF-808 made through a facile method using for fabrication of high-performance mixed matrix composite CO2 capture membranes. Carbon Capture Sci. Technol. 10, 100156. doi:10.1016/j.ccst.2023.100156.

Britt, D., Furukawa, H., Wang, B., Glover, T.G., Yaghi, O.M., 2009. Highly efficient separation of carbon dioxide by a metal-organic framework replete with open metal sites. Proc. Natl. Acad. Sci. 106, 20637–20640.

Wongsakulphasatch, S., Kiatkittipong, W., Saupsor, J., Chaiwiseshphol, J., Piroonlerkgul, P., Parasuk, V., Assabumrungrat, S., 2017. Effect of Fe open metal site in metal-organic frameworks on post-combustion CO2 capture performance. Greenhouse Gases 7, 383–394.

Kökçam-Demir, Ü., Goldman, A., Esrafili, L., Gharib, M., Morsali, A., Weingart, O., Janiak, C., 2020. Coordinatively unsaturated metal sites (open metal sites) in metal–organic frameworks: design and applications. Chem. Soc. Rev. 49, 2751–2798. doi:10.1039/C9CS00609E.

Shang, S., Yang, C., Sun, M., Tao, Z., Hanif, A., Gu, Q., Shang, J., 2022. CO2 capture from wet flue gas using transition metal inserted porphyrin-based metal-organic frameworks as efficient adsorbents. Sep. Purif. Technol. 301, 122058.

Xu, W., Ding, Q., Sang, P., Xu, J., Shi, Z., Zhao, L., Chi, Y., Guo, W., 2015. Effect of modified metal center in ligand for CO2 capture in novel Zr-based porphyrinic metal–organic frameworks: a computational investigation. J. Phys. Chem. C 119, 21943–21951.

Yu, K., Ahmed, I., Won, D.-I., Lee, W.I., Ahn, W.-S., 2020. Highly efficient adsorptive removal of sulfamethoxazole from aqueous solutions by porphyrinic MOF-525 and MOF-545. Chemosphere 250, 126133.

Prasetya, N., Wöll, C., 2023. Removal of diclofenac by adsorption process studied in free-base porphyrin Zr-metal organic frameworks (Zr-MOFs). RSC Adv. 13, 22998–23009.

Deria, P., Gómez-Gualdrón, D.A., Hod, I., Snurr, R.Q., Hupp, J.T., Farha, O.K., 2016. Framework-topology-dependent catalytic activity of zirconium-based (porphinato) zinc (II) MOFs. J. Am. Chem. Soc. 138, 14449–14457.

Kung, C.-W., Chang, T.-H., Chou, L.-Y., Hupp, J.T., Farha, O.K., Ho, K.-C., 2015. Post metalation of solvothermally grown electroactive porphyrin metal–organic framework thin films. Chem. Commun. 51, 2414–2417.

Prasetya, N., Okur, S., 2023. MOF-composite sensors to eliminate the QCM positive frequency shift. Sens. Actuators B, 134507 doi:10.1016/j.snb.2023.134507.

Herrera-Herrera, P.A., Rodríguez-Sevilla, E., Varela, A.S., 2021. The role of the metal center on charge transport rate in MOF-525: cobalt and nickel porphyrin. Dalton Trans. 50, 16939–16944. doi:10.1039/D1DT03435A.

Morris, W., Volosskiy, B., Demir, S., Gándara, F., McGrier, P.L., Furukawa, H., Cascio, D., Stoddart, J.F., Yaghi, O.M., 2012. Synthesis, structure, and metalation of two new highly porous zirconium metal–organic frameworks. Inorg. Chem. 51, 6443–6445. doi:10.1021/ic300825s.

Maxwell, J.C., 1873. A Treatise On Electricity and Magnetism. Oxford: Clarendon Press.

Vinh-Thang, H., Kaliaguine, S., 2013. Predictive models for mixed-matrix membrane performance: a review. Chem. Rev. 113, 4980–5028.

Gomez-Gualdron, D.A., Gutov, O.V., Krungleviciute, V., Borah, B., Mondloch, J.E., Hupp, J.T., Yildirim, T., Farha, O.K., Snurr, R.Q., 2014. Computational design of metal–organic frameworks based on stable zirconium building units for storage and delivery of methane. Chem. Mater. 26, 5632–5639.

Macrae, C.F., Sovago, I., Cottrell, S.J., Galek, P.T., McCabe, P., Pidcock, E., Platings, M., Shields, G.P., Stevens, J.S., Towler, M., 2020. Mercury 4.0: from visualization to analysis, design and prediction. J. Appl. Crystallogr. 53, 226–235.

D.S. Biovia, BIOVIA pipeline pilot, Dassault Systèmes: San Diego, BW, Release (2017).

Dubbeldam, D., Calero, S., Ellis, D.E., Snurr, R.Q., 2016. RASPA: molecular simulation software for adsorption and diffusion in flexible nanoporous materials. Mol. Simul. 42, 81–101.

Mayo, S.L., Olafson, B.D., Goddard, W.A., 1990. DREIDING: a generic force field for molecular simulations. J. Phys. Chem. 94, 8897–8909.

Potoff, J.J., Siepmann, J.I., 2001. Vapor–liquid equilibria of mixtures containing alkanes, carbon dioxide, and nitrogen. AlChE J. 47, 1676–1682.

Eggimann, B.L., Sunnarborg, A.J., Stern, H.D., Bliss, A.P., Siepmann, J.I., 2014. An online parameter and property database for the TraPPE force field. Mol. Simul. 40, 101–105.

Murthy, C., Singer, K., Klein, M., McDonald, I., 1980. Pairwise additive effective potentials for nitrogen. Mol. Phys. 41, 1387–1399.

Martin, M.G., Siepmann, J.I., 1998. Transferable potentials for phase equilibria. 1. United-atom description of n-alkanes. J. Phys. Chem. B 102, 2569–2577.

Rappe, A.K., Goddard III, W.A., 1991. Charge equilibration for molecular dynamics simulations. J. Phys. Chem. 95, 3358–3363.

Ewald, P.P., 1921. Die Berechnung optischer und elektrostatischer Gitterpotentiale. Ann. Phys. 369, 253–287.

Evans, D.J., Holian, B.L., 1985. The nose–hoover thermostat. J. Chem. Phys. 83, 4069–4074.

Frenkel, D., Smit, B., 2023. Understanding Molecular simulation: from Algorithms to Applications. Elsevier.

Einstein, A., 1956. Investigations On the Theory of the Brownian Movement. Courier Corporation.

Erucar, I., Keskin, S., 2011. Screening metal–organic framework-based mixed-matrix membranes for CO2/CH4 separations. Ind. Eng. Chem. Res. 50, 12606–12616.

Budhathoki, S., Ajayi, O., Steckel, J.A., Wilmer, C.E., 2019. High-throughput computational prediction of the cost of carbon capture using mixed matrix membranes. Energy Environ. Sci. 12, 1255–1264.

Su, N.C., Sun, D.T., Beavers, C.M., Britt, D.K., Queen, W.L., Urban, J.J., 2016. Enhanced permeation arising from dual transport pathways in hybrid polymer–MOF membranes. Energy Environ. Sci. 9, 922–931.

Bouma, R., Checchetti, A., Chidichimo, G., Drioli, E., 1997. Permeation through a heterogeneous membrane: the effect of the dispersed phase. J. Memb. Sci. 128, 141–149.

Giovannetti, R., 2012. The use of spectrophotometry UV–Vis for the study of porphyrins. Macro Nano Spectroscopy 87–108.

Streit, H.C., Adlung, M., Shekhah, O., Stammer, X., Arslan, H.K., Zybaylo, O., Ladnorg, T., Gliemann, H., Franzreb, M., Wöll, C., 2012. Surface-anchored MOF-based photonic antennae. ChemPhysChem 13, 2699–2702.

Hadjiivanov, K.I., Panayotov, D.A., Mihaylov, M.Y., Ivanova, E.Z., Chakarova, K.K., Andonova, S.M., Drenchev, N.L., 2020. Power of infrared and raman spectroscopies to characterize metal-organic frameworks and investigate their interaction with guest molecules. Chem. Rev. 121, 1286–1424.

Chi, W.S., Sundell, B.J., Zhang, K., Harrigan, D.J., Hayden, S.C., Smith, Z.P., 2019. Mixed-Matrix membranes formed from multi-dimensional metal–organic frameworks for enhanced gas transport and plasticization resistance. ChemSusChem 12, 2355–2360.

Altintas, C., Keskin, S., 2022. MOF adsorbents for flue gas separation: comparison of material ranking approaches. Chem. Eng. Res. Des. 179, 308–318.

Maserati, L., Meckler, S.M., Bachman, J.E., Long, J.R., Helms, B.A., 2017. Diamine-appended Mg2 (dobpdc) nanorods as phase-change fillers in mixed-matrix membranes for efficient CO2/N2 separations. Nano Lett. 17, 6828–6832.

Adams, R., Carson, C., Ward, J., Tannenbaum, R., Koros, W., 2010. Metal organic framework mixed matrix membranes for gas separations. Microporous Mesoporous Mater. 131, 13–20.
Altintas, C., Keskin, S., 2018. Molecular simulations of MOF membranes and performance predictions of MOF/polymer mixed matrix membranes for CO2/CH4 separations. ACS Sustain. Chem. Eng. 7, 2739–2750.
Comesaña-Gándara, B., Chen, J., Bezzu, C.G., Carta, M., Rose, I., Ferrari, M.-C., Esposito, E., Fuoco, A., Jansen, J.C., McKeown, N.B., 2019. Redefining the Robeson upper bounds for CO 2/CH 4 and CO 2/N 2 separations using a series of ultrapermeable benzotriptycene-based polymers of intrinsic microporosity. Energy Environ. Sci. 12, 2733–2740.
Chen, W., Zhang, Z., Hou, L., Yang, C., Shen, H., Yang, K., Wang, Z., 2020. Metal-organic framework MOF-801/PIM-1 mixed-matrix membranes for enhanced CO2/N2 separation performance. Sep. Purif. Technol. 250, 117198.
Deng, J., Dai, Z., Hou, J., Deng, L., 2020. Morphologically tunable MOF nanosheets in mixed matrix membranes for CO2 separation. Chem. Mater. 32, 4174–4184.
Gong, H., Nguyen, T.H., Wang, R., Bae, T.-H., 2015. Separations of binary mixtures of CO2/CH4 and CO2/N2 with mixed-matrix membranes containing Zn (pyrz) 2 (SiF6) metal-organic framework. J. Memb. Sci. 495, 169–175.
Prasetya, N., Ladewig, B.P., 2018. New Azo-DMOF-1 MOF as a photoresponsive low-energy CO2 adsorbent and its exceptional CO2/N2 separation performance in mixed matrix membranes. ACS Appl. Mater. Interfaces 10, 34291–34301.
Mubashir, M., Yeong, Y.F., Lau, K.K., Chew, T.L., Norwahyu, J., 2018. Efficient CO2/N2 and CO2/CH4 separation using NH2-MIL-53 (Al)/cellulose acetate (CA) mixed matrix membranes. Sep. Purif. Technol. 199, 140–151.
Prasetya, N., Teck, A.A., Ladewig, B.P., 2018a. Matrimid-JUC-62 and Matrimid-PCN-250 mixed matrix membranes displaying light-responsive gas separation and beneficial ageing characteristics for CO2/N2 separation. Sci. Rep. 8, 2944.
Benzaqui, M., Pillai, R.S., Sabetghadam, A., Benoit, V., Normand, P., Marrot, J., Menguy, N., Montero, D., Shepard, W., Tissot, A., 2017. Revisiting the aluminum trimesate-based MOF (MIL-96): from structure determination to the processing of mixed matrix membranes for CO2 capture. Chem. Mater. 29, 10326–10338.
Perez, E.V., Balkus Jr, K.J., Ferraris, J.P., Musselman, I.H., 2009. Mixed-matrix membranes containing MOF-5 for gas separations. J. Memb. Sci. 328, 165–173.
Gao, J., Mao, H., Jin, H., Chen, C., Feldhoff, A., Li, Y., 2020. Functionalized ZIF-7/Pebax® 2533 mixed matrix membranes for CO2/N2 separation. Microporous Mesoporous Mater. 297, 110030.
Lai, W.-H., Zhuang, G.-L., Tseng, H.-H., Wey, M.-Y., 2019. Creation of tiny defects in ZIF-8 by thermal annealing to improve the CO2/N2 separation of mixed matrix membranes. J. Memb. Sci. 572, 410–418.
Zornoza, B., Seoane, B., Zamaro, J.M., Téllez, C., Coronas, J., 2011. Combination of MOFs and zeolites for mixed-matrix membranes. ChemPhysChem 12, 2781–2785.
Zhou, Y., Jia, M., Zhang, X., Yao, J., 2020. Etched ZIF-8 as a filler in mixed-matrix membranes for enhanced CO2/N2 separation. Chemistry 26, 7918–7922.
Rodrigues, M.A., de Souza Ribeiro, J., de Souza Costa, E., de Miranda, J.L., Ferraz, H.C., 2018. Nanostructured membranes containing UiO-66 (Zr) and MIL-101 (Cr) for O2/N2 and CO2/N2 separation. Sep. Purif. Technol. 192, 491–500.
Khdhayyer, M.R., Esposito, E., Fuoco, A., Monteleone, M., Giorno, L., Jansen, J.C., Attfield, M.P., Budd, P.M., 2017. Mixed matrix membranes based on UiO-66 MOFs in the polymer of intrinsic microporosity PIM-1. Sep. Purif. Technol. 173, 304–313.
Wang, H., Ni, Y., Dong, Z., Zhao, Q., 2021a. A mechanically enhanced metal-organic framework/PDMS membrane for CO2/N2 separation. React. Funct. Polym. 160, 104825.
Nik, O.G., Chen, X.Y., Kaliaguine, S., 2012. Functionalized metal organic framework-polyimide mixed matrix membranes for CO2/CH4 separation. J. Memb. Sci. 413, 48–61.
Dorosti, F., Omidkhah, M., Abedini, R., 2014. Fabrication and characterization of Matrimid/MIL-53 mixed matrix membrane for CO2/CH4 separation. Chem. Eng. Res. Des. 92, 2439–2448.
Zhang, Y., Musselman, I.H., Ferraris, J.P., Balkus Jr, K.J., 2008. Gas permeability properties of Matrimid® membranes containing the metal-organic framework Cu–BPY–HFS. J. Memb. Sci. 313, 170–181.
Liu, Y., Liu, G., Zhang, C., Qiu, W., Yi, S., Chernikova, V., Chen, Z., Belmabkhout, Y., Shekhah, O., Eddaoudi, M., 2018a. Enhanced CO2/CH4 separation performance of a mixed matrix membrane based on tailored MOF-polymer formulations. Adv. Sci. 5, 1800982.
Chen, X.Y., Vinh-Thang, H., Rodrigue, D., Kaliaguine, S., 2012. Amine-functionalized MIL-53 metal–organic framework in polyimide mixed matrix membranes for CO2/CH4 separation. Ind. Eng. Chem. Res. 51, 6895–6906.
Guo, X., Huang, H., Ban, Y., Yang, Q., Xiao, Y., Li, Y., Yang, W., Zhong, C., 2015. Mixed matrix membranes incorporated with amine-functionalized titanium-based metal-organic framework for CO2/CH4 separation. J. Memb. Sci. 478, 130–139.
Japip, S., Wang, H., Xiao, Y., Chung, T.S., 2014. Highly permeable zeolitic imidazolate framework (ZIF)-71 nano-particles enhanced polyimide membranes for gas separation. J. Memb. Sci. 467, 162–174.
Shahid, S., Nijmeijer, K., 2014. High pressure gas separation performance of mixed-matrix polymer membranes containing mesoporous Fe (BTC). J. Memb. Sci. 459, 33–44.
Liu, G., Labreche, Y., Chernikova, V., Shekhah, O., Zhang, C., Belmabkhout, Y., Eddaoudi, M., Koros, W.J., 2018b. Zeolite-like MOF nanocrystals incorporated 6FDA-polyimide mixed-matrix membranes for CO2/CH4 separation. J. Memb. Sci. 565, 186–193.
Guo, A., Ban, Y., Yang, K., Yang, W., 2018. Metal-organic framework-based mixed matrix membranes: synergetic effect of adsorption and diffusion for CO2/CH4 separation. J. Memb. Sci. 562, 76–84.
Wang, Z., Yuan, J., Li, R., Zhu, H., Duan, J., Guo, Y., Liu, G., Jin, W., 2021b. ZIF-301 MOF/6FDA-DAM polyimide mixed-matrix membranes for CO2/CH4 separation. Sep. Purif. Technol. 264, 118431.
Rodenas, T., Van Dalen, M., Serra-Crespo, P., Kapteijn, F., Gascon, J., 2014. Mixed matrix membranes based on NH2-functionalized MIL-type MOFs: influence of structural and operational parameters on the CO2/CH4 separation performance. Microporous Mesoporous Mater. 192, 35–42.
Jiang, Y., Liu, C., Caro, J., Huang, A., 2019. A new UiO-66-NH2 based mixed-matrix membranes with high CO2/CH4 separation performance. Microporous Mesoporous Mater. 274, 203–211.
Qian, J., Wu, T., Shi, J., Chang, H., Liu, D., Pan, Y., 2021. Improved CO2/CH4 separation performance of mixed-matrix membrane by adding ZIF-7-NH2 nanocrystals. J. Appl. Polym. Sci. 138, 50424.
Castro-Muñoz, R., Fila, V., Martin-Gil, V., Muller, C., 2019. Enhanced CO2 permeability in Matrimid® 5218 mixed matrix membranes for separating binary CO2/CH4 mixtures. Sep. Purif. Technol. 210, 553–562.
Jomekian, A., Behbahani, R.M., Mohammadi, T., Kargari, A., 2016. CO2/CH4 separation by high performance co-casted ZIF-8/Pebax 1657/PES mixed matrix membrane. J. Nat. Gas Sci. Eng. 31, 562–574.
Bae, T.-H., Long, J.R., 2013. CO 2/N 2 separations with mixed-matrix membranes containing Mg 2 (dobdc) nanocrystals. Energy Environ. Sci. 6, 3565–3569.
Prasetya, N., Donose, B.C., Ladewig, B.P., 2018b. A new and highly robust light-responsive Azo-UiO-66 for highly selective and low energy post-combustion CO 2 capture and its application in a mixed matrix membrane for CO 2/N 2 separation. J. Mater. Chem. A 6, 16390–16402.
Khan, H.R., Jahan, Z., Khan Niazi, M.B., Noor, T., Hou, H., Rafiq, S., 2022. High–Selective separation performance of CO2 from CH4 by Interfacial engineering of ultra-low-dose bimetallic Pyrazine-MOF based mixed matrix membranes. Carbon Capture Sci. Technol. 3, 100048. doi:10.1016/j.ccst.2022.100048.